J. Fluid Mech. (2009), *vol.* 623, *pp.* 283–316.
doi:10.1017/S0022112008004965 Printed in the United Kingdom

A generalized mean-field model of the natural and high-frequency actuated flow around a high-lift configuration

DIRK M. LUCHTENBURG[1]†, BERT GÜNTHER[1], BERND R. NOACK[1], RUDIBERT KING[2] AND GILEAD TADMOR[3]

[1]Department of Fluid Dynamics and Engineering Acoustics, Berlin Institute of Technology MB1, Straße des 17. Juni 135, D-10623 Berlin, Germany

[2]Department of Plant and Process Technology, Berlin Institute of Technology ER2-1, Hardenbergstraße 36a, D-10623 Berlin, Germany

[3]Department of Electrical and Computer Engineering, Northeastern University, 440 Dana Research Building, Boston, MA 02115, USA

(Received 25 October 2007 and in revised form 13 November 2008)

A low-dimensional Galerkin model is proposed for the flow around a high-lift configuration, describing natural vortex shedding, the high-frequency actuated flow with increased lift and transients between both states. The form of the dynamical system has been derived from a generalized mean-field consideration. Steady state and transient URANS (unsteady Reynolds-averaged Navier–Stokes) simulation data are employed to derive the expansion modes and to calibrate the system parameters. The model identifies the mean field as the mediator between the high-frequency actuation and the low-frequency natural shedding instability.

1. Introduction

Periodic excitation is one of the fundamental tools of active flow control (see for example Gad-el-Hak 1996, 2000; King 2007). In particular, separation of the flow over airfoils at high angles of attack can be delayed using periodic actuation (Seifert, Darabi & Wygnanski 1996; Amitay & Glezer 2002; Raju & Mittal 2002; Collis *et al.* 2004; Becker *et al.* 2007). Effective options include high-frequency forcing using synthetic jets and plasma actuators. A flow model of the actuated system is desirable as a test-bed for physical understanding and is necessary for systematic feedback control design. To be useful for feedback design, the model must be both sufficiently simple for feasible real-time implementation, and yet robustly represent the natural and actuated dynamics. In particular, models must be capable of representing the cross-frequency interaction between high-frequency actuation and low-frequency instabilities, and do so with the least feasible number of modes. The current paper proposes a framework for such models. Separation control of the flow around a high-lift configuration with high-frequency actuation serves as a benchmark for the development of a least-order design model using proper orthogonal decomposition (POD) and shift-modes (Noack *et al.* 2003).

† Email address for correspondence: dirk.m.luchtenburg@tu-berlin.de

The high-lift configuration plays an essential role in the take-off and landing performance of large commercial aircrafts, allowing lower landing and take-off speeds and thus shorter runways. Conventionally, such a configuration consists of complex heavy and expensive multi-element high-lift devices. Active separation control is currently studied as a means for more compact and less heavy configurations, or, alternatively, shorter takeoff and landing runs. In Günther *et al.* (2007) the authors present an experimental and numerical investigation, showing that the mean aerodynamic lift of a traditional three-element high-lift configuration can be significantly enhanced by means of open-loop periodic excitation. As recently shown by the authors (Pastoor *et al.* 2006; Henning *et al.* 2007; Pastoor *et al.* 2008), the efficiency and efficacy of periodic actuation can be significantly improved by closing the loop in flow control using sensor measurements. Building on these results, the modelling framework suggested here is intended as an enabler for subsequent model-based optimized and closed-loop design.

Low dimension and simplicity are key enablers in design-accessible flow models. The Galerkin method, and more specifically, the POD Galerkin model (see Holmes, Lumley & Berkooz 1998) is particularly appealing and widely used due to the optimal efficiency in representing the dynamics of globally dominant coherent flow structures. This strength is also a serious weakness when associated with periodic zero-net-mass-flux actuation, such as the one considered in the current paper. One issue is the fact that the interaction between the very local actuation and the globally dominant coherent structures is mediated by a succession of small structures and convective effects that the POD Galerkin framework is expressly designed to ignore. For example, a direct inclusion of actuation, e.g. as a local volume force, will have only a diminishingly small contribution to the Galerkin projection of the Navier–Stokes equations onto the Galerkin basis. This is commonly addressed by identifying the periodic actuation not with its immediate, local effect, but with locked-in forcing effects on globally synchronized coherent structures associated with dynamics at the actuation frequency (Noack, Tadmor & Morzyński 2004*c*). Time-scale separation often allows to algebraically associate the forcing effect on the Fourier coefficients of these modes with the direct and quadrature components of the actuation command. The terminology is borrowed from power engineering, where the *direct* signal is aligned with the sinusoidal reference, and the *quadrature* is time shifted by a quarter period. The coefficients of this relationship, included in the control input term of the actuated Galerkin model, are calibrated with empirical data as by Tadmor *et al.* (2004).

A subsequent challenge arises when the actuation frequency is different, worse yet, incommensurate with the frequency of the controlled phenomenon. Typically, the actuation frequency is not harmonically related to the shear-layer frequency, and is higher than the vortex-shedding frequency (Raju & Mittal 2002; Günther *et al.* 2007). A low-dimensional model representing each of the leading harmonics by a mode pair naturally accommodates amplitude and phase manipulations. Quadratic nonlinearity allows to enrich this repertoire with frequency doubling and time variations. Yet, very low-order models, based, e.g. on POD analysis of natural and actuated attractors, are incapable of capturing the energy transfer between mode pairs that represent unrelated frequencies. Even more so, the phase-independent open-loop stabilizing effect of high-frequency actuation cannot be explained by direct mode interactions – even when the actuation and the instability frequencies are harmonically related. This difficulty is sharpened in the fairly common case, encountered in the current discussion, where dominant coherent structures associated with different frequencies do not have

significant spatial overlap. At the centre of the current developments is an outline of the direct derivation of a mean-field model that accommodates multi-frequency fluctuations, and of a subsequent counterpart in the Galerkin framework.

The model proposed in this note builds on the mean-field theory, as developed by Noack *et al.* (2003). The underlying ideas trace back to Stuart's work (1958), and more recently, to Maurel, Pagneux & Wesfreid (1995) and Zielinska *et al.* (1997) where the critical role of the time-varying base flow in saturating instabilities is elaborated. The coupling between saturation amplitudes and base flow is communicated by the Reynolds equation. This equation establishes the momentum balance between fast fluctuations and base flow changes, captured by the Reynolds stress. Along with linear instabilities, this energy balance is indeed a fundamental component of flow dynamics. As shown by Noack *et al.* (2003) (see also Tadmor *et al.* 2007), mean-field dynamics can be effectively captured by a single *shift-mode*, and its inclusion is essential to a low-order (and minimum) POD Galerkin representation of natural transients and subsequently to control-oriented models (Gerhard *et al.* 2003; Luchtenburg *et al.* 2006; Siegel *et al.* 2008).

Here, we postulate two mean-field modes, capturing energy exchanges between mean flow structures and the fluctuations at the natural and the actuated frequencies. The fact that fluctuations at the actuated frequency are naturally stable reflects, in this context, a higher stabilizing effect of the mean-field changes induced at that frequency, than those due to the natural instability. Consequently, the forced amplification of the fluctuations at the actuated frequency, and of entailed base flow changes, leads to the desired and observed attenuation of the natural instability. The mean-field modes are therefore proposed as the missing component, mediating between the high-frequency actuation and the natural lower frequency instability. The model is validated and calibrated, using flow data of unsteady Reynolds-averaged Navier–Stokes (URANS) simulations. As will be seen, the mean-field POD model is capable to predict the effect of actuation on both the velocity field and on the associated lift coefficient.

The paper is organized as follows. The benchmark system and its URANS simulation are described in § 2. The mechanism of high-frequency forcing is elucidated with an introductory example in § 3. The mean-field model is derived first in the original context of the Navier–Stokes equation (NSE) in § 4. The least-order Galerkin model that describes the transient and post-transient dynamics of the natural and actuated flow is derived in § 5. In § 6, we compare the CFD simulation with the prediction of the least-order Galerkin model. A discussion of the Galerkin-model is provided in § 7. The main findings and their implications are summarized in § 8.

2. Numerical simulation

In this section, the benchmark simulation of the flow around the high-lift configuration is outlined, including the configuration (§ 2.1), the simulation (§ 2.2) and the flow properties (§ 2.3).

2.1. *Configuration*

We consider the incompressible two-dimensional flow over the swept constant chord half (SCCH) high-lift configuration (see figure 1). This configuration is employed in several experimental and numerical studies targeting passive and active flow control (Kaepernick, Koop & Ehrenfried 2005; Schatz, Günther & Thiele 2006; Günther

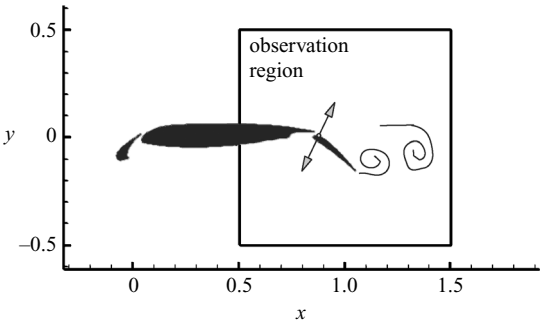

FIGURE 1. A sketch of the three-element high-lift configuration and the observation region for the model. Periodic excitation (↔) is implemented at the upper part of the trailing edge flap.

et al. 2007). The control goal in these studies includes lift enhancement as well as noise suppression.

The chord length of the configuration, with retracted high-lift devices, is denoted by c. The three-component setup consists of a main airfoil equipped with a leading edge slat and a trailing edge flap with relative chord lengths of $c_{sl} = 0.158\,c$ and $c_{fl} = 0.254\,c$, respectively. Henceforth, all physical variables are assumed non-dimensionalized with respect to the chord length c, the incoming flow velocity U_∞ and the constant density ρ. The flow is considered at the Reynolds number of $Re = U_\infty\, c/\nu = 10^6$ (ν: kinematic viscosity of the fluid). The slat deflection angle is set to 26.5°, the flap deflection angle to 37° and the angle of attack of the main wing section is 6°. At these conditions, the flow remains attached over the slat and the main wing section, but is fully separated over the flap. Then, the wake is characterized by the periodic generation and alternate shedding of leading and trailing edge vortices.

Periodic actuation is introduced via a zero-net-mass-flux actuator on a small wall section at the upper side of the trailing edge flap. The imposed flow velocity is orthogonal to the wall and is located at $0.04\,c$ behind the leading edge of the flap (see figure 1). The actuation velocity is prescribed by

$$b(t) = B\cos(\Omega^a t), \tag{2.1}$$

where Ω^a is the angular actuation frequency and B the amplitude of actuation. This frequency is given by

$$\Omega^a = 2\pi St^a,$$

where $St^a = f^a c/U_\infty$ represents the Strouhal number with the actuation frequency f^a. The Strouhal number for natural (un-actuated) vortex-shedding frequency f^n is analogously defined, $St^n = f^n c/U_\infty$. Experimental and computational studies of flows around high-lift configurations often non-dimensionalize the frequencies with the flap length c_{fl} as opposed to the cord length c. Hence, we introduce $St_{fl} = f c_{fl}/U_\infty = (c_{fl}/c)\,St$ with applicable superscripts 'n' and 'a' for later reference.

The actuation intensity is characterized by the non-dimensional momentum coefficient

$$C_\mu = \frac{H}{c}\left(\frac{B}{U_\infty}\right)^2,$$

where H is the slot width ($H = 0.001238\,c_{fl}$).

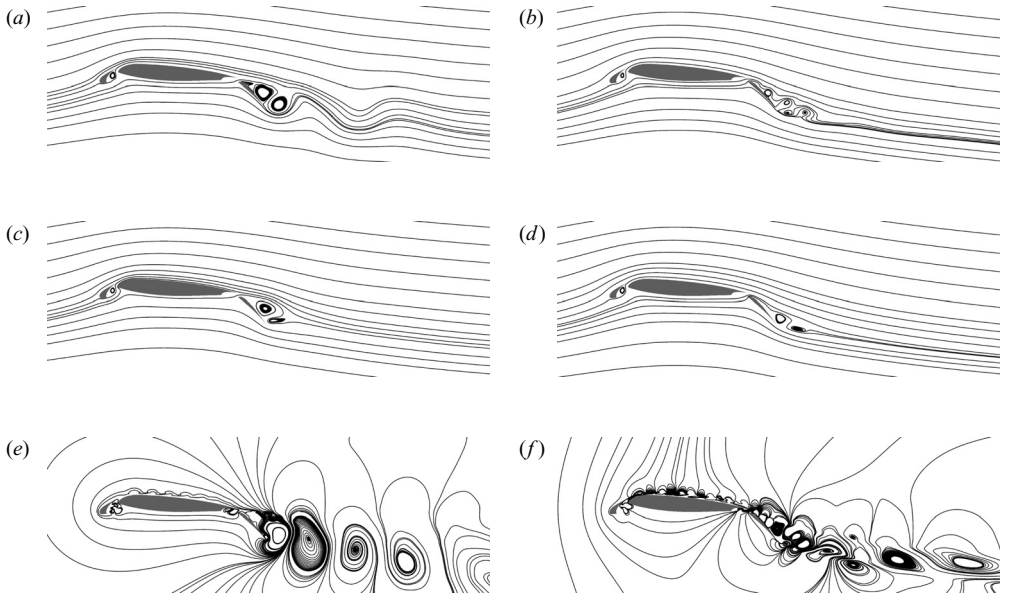

FIGURE 2. Comparison of a natural (*a*, *c*, *e*) and an actuated snapshot (*b*, *d*, *f*). The top row (*a*, *b*) shows a characteristic snapshot that is Reynolds decomposed into the respective attractor mean (*c*, *d*) and instantaneous fluctuation (*e*, *f*). The flow field is visualized by streamlines.

2.2. *Unsteady Reynolds-averaged Navier–Stokes simulation*

The two-dimensional coherent structure dynamics are resolved by URANS equation. Small-scale turbulent fluctuations are incorporated by the LLR k-ω model (Rung & Thiele 1996). The URANS equation is discretized by an incompressible finite-volume scheme of second-order accuracy in space and time. The numerical data used here have been obtained with the numerical code *ELAN* developed at the Computational Fluid Dynamics and Aeroacoustics Group (Professor F. Thiele) at the Berlin Institute of Technology. The computational domain extends $15\,c$ upstream, above and below the airfoil and $25c$ downstream. This domain is discretized on a multi-block structured mesh into 90 000 cells. The non-dimensional wall distance of the first cell centre is kept below $y^+ = 1$ over the entire surface.

2.3. *Natural and periodically forced flow*

The unactuated flow field around the trailing edge flap is characterized by massive separation. The left side of figure 2 shows a characteristic snapshot and its Reynolds decomposition. The dead-water zone is associated with periodic vortex shedding above the upper surface of the flap. The spectrum of the lift coefficient reveals a dominant Strouhal number of $St^n_{fl} = f^n c_{fl}/U_\infty = 0.32$ corresponding to that vortex shedding.

Actuation is added to the configuration at natural flow conditions. A parameter study shows that, under periodic actuation, lift is maximized at a momentum coefficient of $C_\mu = 400 \times 10^{-5}$ and an excitation frequency of $St^a_{fl} = 0.6$. In this case, the lift coefficient is increased by 19%. For the modelling task, we set $St^a_{fl} = 0.6$ and $C_\mu = 114 \times 10^{-5}$. This results in a lift increase of about 15% at an actuation frequency that is 1.88 times larger than the natural shedding frequency, i.e. $St^a_{fl}/St^n_{fl} = 1.88$. The effect on the flow field is the near complete attenuation of fluctuations at the

natural frequency, and the emergence of a new attractor, locked-in on the actuation frequency. The right side of figure 2 shows a characteristic snapshot of the actuated flow. Spatially, the natural oscillations are most pronounced in the wake actuated fluctuations are concentrated above and near the trailing edge flap.

3. Phenomenological modelling

In this section, the lift-increasing effect of high-frequency forcing is phenomenologically modelled. Simple arguments will lead us to the same form of the dynamical systems as a more elaborate derivation from the Navier–Stokes equation in subsequent sections.

The dynamical system shall describe the following four aspects of the URANS simulations:

(i) von Kármán vortex shedding without actuation;
(ii) lock-in shear-layer shedding under high-frequency forcing;
(iii) the transient from state (i) to state (ii) under forcing and
(iv) the transient from (ii) to (i) when forcing is turned off.

Oscillatory flows are characterized by an amplitude A and phase α. These quantities can be considered as polar coordinates of the phase space $(a_1, a_2) = A\ [\cos\alpha, \sin\alpha]$. Superscripts '$n$' and '$a$' refer to the natural and actuated state, respectively.

The self-amplified amplitude-limited behaviour of vortex shedding may be described by the Landau equation (Noack *et al.* 2003),

$$\dot{a}_1^n = \tilde{\sigma}^n\, a_1^n - \omega^n\, a_2^n, \tag{3.1a}$$

$$\dot{a}_2^n = \omega^n\, a_1^n + \tilde{\sigma}^n\, a_2^n, \tag{3.1b}$$

$$\tilde{\sigma}^n = \sigma^n - \sigma^{n,n}\ (A^n)^2\,, \tag{3.1c}$$

where σ^n denotes the positive growth rate, $\sigma^{n,n}$ the positive Landau constant and as noted above, $A^n = \sqrt{(a_1^n)^2 + (a_2^n)^2}$ the amplitude. For reasons of simplicity, the frequency ω^n is assumed as constant.

The shear-layer dynamics is excited by high-frequency forcing with amplitude B, phase β and frequency $\dot{\beta} = \omega^a$. The phase difference of the actuation signal with respect to the oscillation of the flow is given by θ. This behaviour is most easily represented by a linear damped oscillator with a periodic forcing at the eigenfrequency:

$$\dot{a}_1^a = \sigma^a\, a_1^a - \omega^a\, a_2^a + g\ \ B\cos(\theta + \beta), \tag{3.2a}$$

$$\dot{a}_2^a = \omega^a\, a_1^a + \sigma^a\, a_2^a + g\ \ B\sin(\theta + \beta). \tag{3.2b}$$

Here, σ^a denotes a negative growth-rate and g the gain of actuation.

We comprise both oscillations in a four-dimensional phase space

$$[a_1,\quad a_2,\quad a_3,\quad a_4] \stackrel{\text{def}}{=} \left[a_1^n,\quad a_2^n,\quad a_1^a,\quad a_2^a\right]$$

with (3.1) and (3.2) governing the joint evolution of these variables. If $B \equiv 0$, then $a_3 = a_4 \equiv 0$, and the resulting system describes the natural flow, according to (i). By (ii), the oscillation at the natural frequency is suppressed when forcing $B > 0$ is employed. This can be achieved by decreasing the growth rate of the natural amplitude, eventually leading to damping, with the growth of the high-frequency amplitude $A^a = \sqrt{(a_1^a)^2 + (a_2^a)^2}$. In complete analogy to the damping term of Landau's model, we add $-\sigma^{n,a}\ (A^a)^2$ to (3.1*c*) following a similar reasoning (see §4). The coefficient is chosen to be $\sigma^{n,a} > \sigma^n/(A^{a,a})^2$, where $A^{a,a}$ is the constant

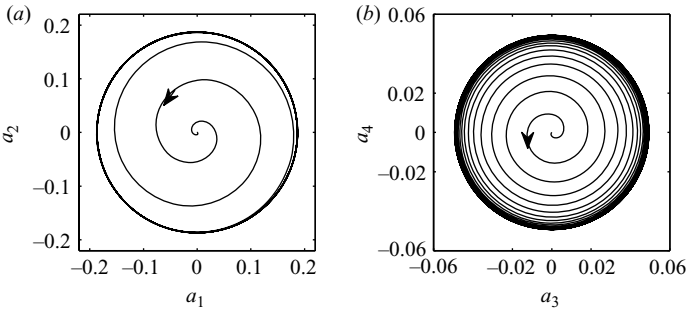

FIGURE 3. Solution of the model problem (3.3) starting from the initial condition $[a_1, a_2, a_3, a_4] = [0.187, 0, 0, 0]$ with actuation. (*a*) The phase portrait of the first oscillator (a_1, a_2); (*b*) the phase portrait (a_3, a_4) of the second oscillator.

value of the amplitude A^a at the forced state. This choice guarantees $\tilde{\sigma}^n < 0$ for all $A^n > 0$ at $A^a = A^{a,a}$. Thus, the limit values $a_1 = a_2 \equiv 0$ are reached at the forced state, according to (ii). In summary, the following system of two coupled oscillators describes the observed behaviour of the natural and actuated states as well as the transients between them, described by properties (i)–(iv):

$$\dot{a}_1 = \tilde{\sigma}^n a_1 - \omega^n a_2, \tag{3.3a}$$

$$\dot{a}_2 = \omega^n a_1 + \tilde{\sigma}^n a_2, \tag{3.3b}$$

$$\dot{a}_3 = \sigma^a a_3 - \omega^a a_4 + g\ \ B\cos(\theta + \beta), \tag{3.3c}$$

$$\dot{a}_4 = \omega^a a_3 + \sigma^a a_4 + g\ \ B\sin(\theta + \beta), \tag{3.3d}$$

$$\tilde{\sigma}^n = \sigma^n - \sigma^{n,n}\,(A^n)^2 - \sigma^{n,a}\,(A^a)^2\,. \tag{3.3e}$$

The reader is reminded that these equations will be analytically justified and re-derived from the Navier–Stokes equation, in the following sections. For a qualitative discussion, we adopt the identified parameters of table 3. Figure 3 shows a solution of (3.3) for an actuated transient from natural to actuated state with periodic forcing starting at time $t = 0$. The qualitative behaviour is as expected, exhibiting a decaying natural oscillation and an excited forced one.

The competition between natural and actuated oscillators can be inferred from (3.3*e*). During a slow transient, the time derivatives of the amplitudes A^n and A^a are arbitrarily small and can be neglected, including $\tilde{\sigma}^n = 0$. Thus, the dependency between both amplitudes is described by

$$\sigma^n = \sigma^{n,n}\,(A^n)^2 + \sigma^{n,a}\,(A^a)^2\,. \tag{3.4}$$

The associated energies are linearly related. One energy can only increase at the expense of the other. Hence, the lift coefficient can be considered as a function of either amplitude. From URANS data, it is observed to increase with the amplitude of actuation.

Figure 4 shows the increase of A^a under forcing (figure 4*a*), corroborates approximately (3.4) (see the quarter ellipse in figure 4*b*) – even for a fast transient – and shows the increase of the lift during the transient (figure 4*c*).

4. Mean-field theory for multi-frequency fluctuations

Here, we discuss the structure of a mean-field model for our benchmark, as implied by an analysis of the flow's governing Navier–Stokes equation. The model will reveal

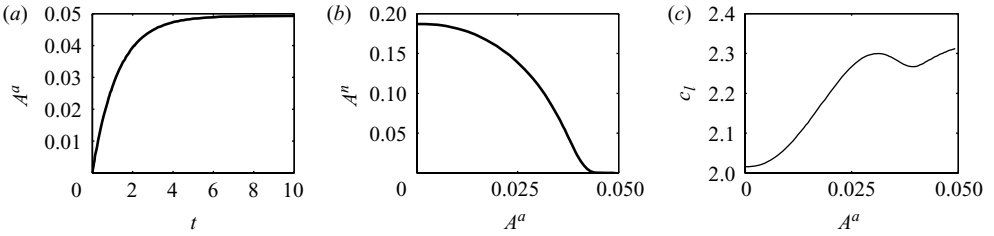

FIGURE 4. Amplitude and lift dynamics for the transient displayed in figure 3. Note that (*a*) A^a increases with time, (*b*) A^n decreases with increasing A^a and (*c*) c_l increases with increasing A^a. The non-monotonous behaviour of $c_l(A^a)$ is an overshoot phenomenon related to the fast transient.

the role of mean-field dynamics in stabilizing an attractor and as a mediator between high-frequency actuation and natural vortex shedding.

Starting with nomenclature, we denote the computational domain by $\Omega \subset \Re^2$. Points in Ω are described in a Cartesian coordinate system, $\boldsymbol{x} = (x, y)$, where the x-axis is aligned with the flow and the y-axis with the transverse direction. The origin is at the leading edge of the configuration (with retracted high-lift devices). Similarly, the velocity field is denoted by $\boldsymbol{u} = (u, v)$, where u and v are components aligned with the x- and y-direction. The velocity field is embedded in the Hilbert space $\mathscr{L}_2(\Omega)$ of square-integrable functions, associated with the standard inner product between two vector fields $\boldsymbol{f}$ and $\boldsymbol{g}$

$$(\boldsymbol{f}, \boldsymbol{g})_\Omega \stackrel{\text{def}}{=} \int_\Omega \mathrm{d}V \; \boldsymbol{f} \cdot \boldsymbol{g}. \tag{4.1}$$

For later reference, we define the inner product between two matrix-valued fields $\boldsymbol{A} = (A_{ij})$ and $\boldsymbol{B} = (B_{ij})$,

$$(\boldsymbol{A}, \boldsymbol{B})_\Omega \stackrel{\text{def}}{=} \int_\Omega \mathrm{d}V \; \boldsymbol{A} : \boldsymbol{B}, \tag{4.2}$$

where the colon ':' denotes double contraction; here: $\boldsymbol{A} : \boldsymbol{B} \stackrel{\text{def}}{=} \sum_{i,j=1}^{2} A_{ij} B_{ji}$. The norm of a vector field is denoted by $\|\boldsymbol{f}\|_\Omega \stackrel{\text{def}}{=} \sqrt{(\boldsymbol{f}, \boldsymbol{f})_\Omega}$. In particular, the instantaneous kinetic energy of a velocity field $\boldsymbol{u}$ is defined by $K \stackrel{\text{def}}{=} \|\boldsymbol{u}\|_\Omega^2/2$.

The incompressible flow is governed by the equation of continuity

$$\nabla \cdot \boldsymbol{u} = 0 \tag{4.3}$$

and the Navier–Stokes equation

$$\mathscr{N}[\boldsymbol{u}] \stackrel{\text{def}}{=} \partial_t \boldsymbol{u} + \nabla \cdot (\boldsymbol{u} \otimes \boldsymbol{u}) + \nabla p - \nu \triangle \boldsymbol{u} - \boldsymbol{g}^a = 0. \tag{4.4}$$

Here, $\nu \stackrel{\text{def}}{=} 1/Re$ is the non-dimensionalized kinematic viscosity, i.e. the reciprocal of the Reynolds number. Boundary actuation effects the flow as an unsteady boundary condition for the velocity field $\boldsymbol{u}$. One example is the zero-net-mass-flux actuation considered in this paper. For reasons of generality, a time-periodic and space-dependent volume force $\boldsymbol{g}^a(\boldsymbol{x}, t)$ is also included. The Navier–Stokes operator $\mathscr{N}$ is only a function of the velocity field, since the pressure field p is a function of the velocity field – modulo a constant.

As a first element of mean-field theory, the ensemble average is introduced and denoted by an overbar, e.g. $\overline{\boldsymbol{u}}$. An approximation of this Reynolds average may be

the running average over a time period T,

$$\overline{\boldsymbol{u}}(t) = \frac{1}{T}\int_{-\frac{T}{2}}^{\frac{T}{2}} \mathrm{d}\tau\ \boldsymbol{u}(t+\tau). \tag{4.5}$$

A discussion of this computation is provided in Appendix A.

Based on the observed phenomenology of the flow, we make the following simplifying assumption.

Assumption NSE 1 (A generalized Krylov–Bogoliubov ansatz). *The velocity field is dominated by the sum of a slowly varying base flow and two oscillatory components which are nearly pure harmonics at the natural and the actuation frequency. Other temporal harmonics are negligible. Thus,*

$$\boldsymbol{u}(\boldsymbol{x}, t) = \boldsymbol{u}^B(\boldsymbol{x}, t) + \boldsymbol{u}^n(\boldsymbol{x}, t) + \boldsymbol{u}^a(\boldsymbol{x}, t), \tag{4.6}$$

where the superscripts B, n and a are respectively used to denote terms related to the slowly varying base flow component, to oscillations at the natural shedding frequency and to oscillations at the actuation frequency. Here, $\boldsymbol{u}^B$ satisfies the steady, inhomogeneous boundary conditions, $\boldsymbol{u}^n$ the homogenized version and $\boldsymbol{u}^a$ accounts for the residual to the unsteady boundary conditions, in particular, those associated with the actuation.

This ansatz implies – in analogy to the Reynolds decomposition – that the fluctuations have vanishing ensemble averages,

$$\overline{\boldsymbol{u}^B} = \boldsymbol{u}^B, \quad \overline{\boldsymbol{u}^n} = 0, \quad \overline{\boldsymbol{u}^a} = 0. \tag{4.7}$$

Following Dušek, Le Gal & Fraunié (1994), the assumed slow variation of the mean flow and the oscillation amplitudes, frequencies and phase shifts can be formalized by introducing a small parameter $\epsilon \ll 1$ and slowly varying amplitude functions $\boldsymbol{u}_0^B$, $\boldsymbol{u}_{1,2}^n$, $\boldsymbol{u}_{1,2}^a$, such that

$$\boldsymbol{u}^B(\boldsymbol{x}, t) = \boldsymbol{u}_0^B(\boldsymbol{x}, \epsilon t), \tag{4.8a}$$

$$\boldsymbol{u}^n(\boldsymbol{x}, t) = \boldsymbol{u}_1^n(\boldsymbol{x}, \epsilon\, t)\ \cos(\Omega^n\, t) + \boldsymbol{u}_2^n(\boldsymbol{x}, \epsilon\, t)\ \sin(\Omega^n\, t), \tag{4.8b}$$

$$\boldsymbol{u}^a(\boldsymbol{x}, t) = \boldsymbol{u}_1^a(\boldsymbol{x}, \epsilon\, t)\ \cos(\Omega^a\, t) + \boldsymbol{u}_2^a(\boldsymbol{x}, \epsilon\, t)\ \sin(\Omega^a\, t), \tag{4.8c}$$

where the angular frequency is defined as $\Omega = 2\pi St$ with applicable superscripts 'n' and 'a'. The reciprocal of the small parameter, i.e. $1/\epsilon$, is assumed to be the characteristic time scale on which the amplitude functions change. This ansatz implies, for instance, that time derivatives of the amplitude functions are of order $O(\epsilon)$, which shall be neglected in the present discussion.

A second simplifying assumption is

Assumption NSE 2 (A non-commensurability ansatz). *There is no direct interaction between $\boldsymbol{u}^n$ and $\boldsymbol{u}^a$ via the quadratic Navier–Stokes term $\nabla\cdot(\boldsymbol{u}\otimes\boldsymbol{u})$.*

This assumption is supported by the numerically observed fact that the natural and actuated oscillations are not harmonically related by integral or half-integral ratios. An even stronger corroboration comes from the observation that the activity regions of these fluctuations rarely overlap. Finally, on each of the two respective attractors, fluctuations in the other frequency are negligible.

We substitute the Krylov–Bogoliubov ansatz NSE 1 into the Navier–Stokes equation and sort terms by the 0th harmonic and the first harmonics at frequency St^n and St^a.

Employing the above approximations yields

$$0 = \nabla\cdot(\boldsymbol{u}^B\otimes\boldsymbol{u}^B) + \nabla\cdot\overline{(\boldsymbol{u}^n\otimes\boldsymbol{u}^n)} + \nabla\cdot\overline{(\boldsymbol{u}^a\otimes\boldsymbol{u}^a)} + \nabla p^B - \nu\,\triangle\boldsymbol{u}^B, \tag{4.9a}$$

$$\partial_t\boldsymbol{u}^n = -\nabla\cdot(\boldsymbol{u}^n\otimes\boldsymbol{u}^B) - \nabla\cdot(\boldsymbol{u}^B\otimes\boldsymbol{u}^n) - \nabla p^n + \nu\,\triangle\boldsymbol{u}^n, \tag{4.9b}$$

$$\partial_t\boldsymbol{u}^a = -\nabla\cdot(\boldsymbol{u}^a\otimes\boldsymbol{u}^B) - \nabla\cdot(\boldsymbol{u}^B\otimes\boldsymbol{u}^a) - \nabla p^a + \nu\,\triangle\boldsymbol{u}^a + \boldsymbol{g}^a. \tag{4.9c}$$

Note that mixed quadratic terms such as $\nabla\cdot(\boldsymbol{u}^a\otimes\boldsymbol{u}^n)$ are eliminated in all equations. In (4.9*a*), that elimination does not require assumption NSE 2 and can be obtained for $St^n \neq St^a$ by the projection (A 1*a*), as explained in the Appendix.

In (4.9*b*, *c*), we invoke the simplifying assumption NSE 2. The temporal behaviours of the quadratic terms $\nabla\cdot(\boldsymbol{u}^B\otimes\boldsymbol{u}^B)$, $\nabla\cdot(\boldsymbol{u}^n\otimes\boldsymbol{u}^n)$ and $\nabla\cdot(\boldsymbol{u}^a\otimes\boldsymbol{u}^a)$ are characterized by the zero and respective second harmonics of the two frequencies. These terms are averaged out by the Krylov–Bogoliubov ansatz or can be filtered out by the windowed projections (A 1*b*) and (A 1*c*) in the Appendix. This explains the absence of these terms from (4.9*b*) and (4.9*c*). The terms $(\boldsymbol{u}^n\otimes\boldsymbol{u}^B)$, $(\boldsymbol{u}^B\otimes\boldsymbol{u}^n)$, $(\boldsymbol{u}^a\otimes\boldsymbol{u}^B)$ and $(\boldsymbol{u}^B\otimes\boldsymbol{u}^a)$ are associated with time oscillations at the natural and actuated frequencies, and are therefore invariant under the respective projections.

Together, the three coupled equations (4.9) constitute mean-field equations at the Navier–Stokes equation level. This model is the cornerstone of the developments in this paper and of the mean-field Galerkin model, that is developed in § 5. Contrary to the original mean-field theory of Stuart (1958), we do not assume weakly nonlinear instability and closeness to the steady Navier–Stokes solution.

We make the next two assumptions in preparation for the presentation of the reduced-order Galerkin model.

Assumption NSE 3 (Phase invariance). *The decomposition (4.6) is phase invariant. By this we mean that the simplified dynamics (4.9) remains valid when* $\boldsymbol{u}^n(\boldsymbol{x},t)$, $\boldsymbol{u}^a(\boldsymbol{x},t)$ *and the actuation command* $b(t)$ *are substituted by* $\boldsymbol{u}^n(\boldsymbol{x},t+\tau_n)$, $\boldsymbol{u}^a(\boldsymbol{x},t+\tau_a)$ *and* $b(t+\tau_a)$ *for arbitrary time shifts* τ_n *and* τ_a. *The actuation command may be the amplitude of the volume force* $\boldsymbol{g}^a$ *or the employed boundary actuator.*

Note that only relative time shifts between the three components are significant. Hence, there is no added generality if we allow time shift also in the base flow (i.e. such a time shift can be factored out by shifting the entire time axis). We call this hypothesis *phase invariance* since time shifts are immediately translated to independent phase shifts of oscillations in the respective two frequencies. We do not assume arbitrary phase shifts between the actuation b and $\boldsymbol{u}^a$, since $\boldsymbol{u}^a$ is interacting with, and eventually locked in, on the actuation. The phase invariance hypothesis is feasible due to the lack of direct phase-dependent interactions between the two oscillatory flow components. It is often a reasonable approximation in POD models for vortex-shedding phenomena. Phase invariance assures that the averaging procedure implied in the simplified dynamics (4.9) yields meaningful results. Counter examples of non-phase-invariant systems are provided in Noack & Copeland (2000).

Assumption NSE 4 (Linearized Reynolds equation). *We assume that the Reynolds equation (4.9a) can be linearized around the steady solution* $\boldsymbol{u}^s$. *Let* $\boldsymbol{u}^B = \boldsymbol{u}^s + \boldsymbol{u}^\Delta$. *The linearized Reynolds equation for the mean-field correction* $\boldsymbol{u}^\Delta$ *is obtained by substitution in (4.9a), subtracting the steady Navier–Stokes equation and neglecting quadratic terms in* $\boldsymbol{u}^\Delta$:

$$0 = \nabla\cdot(\boldsymbol{u}^s\otimes\boldsymbol{u}^\Delta) + \nabla\cdot(\boldsymbol{u}^\Delta\otimes\boldsymbol{u}^s) + \nabla\cdot\overline{(\boldsymbol{u}^n\otimes\boldsymbol{u}^n)} + \nabla\cdot\overline{(\boldsymbol{u}^a\otimes\boldsymbol{u}^a)} + \nabla p^\Delta - \nu\,\triangle\boldsymbol{u}^\Delta. \tag{4.10}$$

This assumption implies that there is a linear relationship between the Reynolds stresses and the mean-field correction. The mere purpose of this assumption is to simplify expressions in the Galerkin model we shall present in § 5. It is stressed that our results readily extend to the more general case, where we appeal to the nonlinear Reynolds equation in its original form. The price paid for that generality is the inclusion of higher-order terms in the expression for the mean-field correction, as will be explained in § 5.

We conclude highlighting some significant observations associated with the mean-field equations (4.9).

(i) The dynamic base flow is effected by two independent Reynolds stresses (hence vector field orientations) yielding the volume forces $\nabla\cdot\overline{(\boldsymbol{u}^n\otimes\boldsymbol{u}^n)}$ and $\nabla\cdot\overline{(\boldsymbol{u}^a\otimes\boldsymbol{u}^a)}$.

(ii) In the un-actuated natural flow, $\boldsymbol{u}^a$ is negligible. In that case, the mean-field model highlights the dynamic interactions and energy exchange between the base flow $\boldsymbol{u}^B$ and the periodic fluctuation $\boldsymbol{u}'=\boldsymbol{u}^n$. The latter induces a mean-field change $\boldsymbol{u}^\Delta$ via the respective Reynolds-stress term, whereas the former acts as either a stabilizing agent for high-level fluctuations or a destabilizing agent for a nearly steady flow, via the terms $\nabla\cdot\left(\boldsymbol{u}^n\otimes\boldsymbol{u}^B+\boldsymbol{u}^B\otimes\boldsymbol{u}^n\right)$. Over the attractor, the flow balances this two-way energy exchange with dissipation. This is the essence of the traditional mean-field model, and the basis for the development of the mean-field Galerkin model in Noack *et al.* (2003).

(iii) The mechanism by which $\boldsymbol{u}^a$ interacts with the mean-field is structured in complete analogy to the natural instability. However, the fact that $\boldsymbol{u}^a$ is negligible without actuation suggests that the total power into $\boldsymbol{u}^a$ from production, dissipation and convection alone acts as a sink and that actuation power is required to maintain the lock-in oscillation. In particular, the Reynolds stress due to $\boldsymbol{u}^a$ gives rise to base flow changes that do not change this stabilizing, energy absorbing effect on $\boldsymbol{u}^a$.

(iv) Of the three equations (4.9*a*), (4.9*b*) and (4.9*c*), the actuated unsteady boundary condition as well as volume force actuator effects directly only (4.9*c*). The actuation-induced oscillations in $\boldsymbol{u}^a$ can interact with (and suppress) the instability at the natural frequency, only by using the varying base flow $\boldsymbol{u}^B$ as a mediating agent. The Reynolds stress due to the excited $\boldsymbol{u}^a$ changes $\boldsymbol{u}^B$, and the change in $\boldsymbol{u}^B$ has a stabilizing effect on $\boldsymbol{u}^n$, despite the counter-acting effect of $\boldsymbol{u}^n$ on $\boldsymbol{u}^B$, via its own Reynolds-stress contribution. This key observation therefore provides the sought mechanism for cross-frequency actuation. In particular, it explains the phase independence of this stabilizing effect, hence the ability to suppress shedding with open-loop actuation.

Our decomposition of the flow field into a base flow and two non-commensurable frequency contributions is formally very similar to the triple decomposition in Reynolds & Hussain (1972) into the base flow, the coherent-structure contribution and the stochastic contribution. Not surprisingly, the balance equations for the triple decomposition are equivalent at steady-state condition.

5. Mean-field Galerkin model

In this section, the mean-field model of § 4 is transcribed into the least-order Galerkin model that is capable to resolve the key flow processes in our benchmark. The discussion begins with a brief review of the Galerkin method in § 5.1. In § 5.2, we discuss the implications of the mean-field model on a Galerkin approximation with a minimal number of modes. The associated Galerkin system of ordinary differential equations is derived in § 5.3.

5.1. *The Galerkin method*

The Galerkin method (see, e.g. Ladyzhenskaya 1963; Fletcher 1984; Holmes *et al.* 1998) is based on a Galerkin expansion of the form

$$\boldsymbol{u}(\boldsymbol{x},t)=\sum_{i=0}^{N}a_i(t)\,\boldsymbol{u}_i(\boldsymbol{x}), \tag{5.1}$$

where $\boldsymbol{u}_0(\boldsymbol{x})$ is a steady base flow (e.g. the attractor mean or the steady solution of the Navier–Stokes equation) and $\{\boldsymbol{u}_i\}_{i=1}^{N}\subset\mathscr{L}_2(\Omega)$ is an orthonormal basis. Time dependency is described by the Fourier coefficients a_i. Following a notation of Rempfer & Fasel (1994), $a_0\equiv 1$ by definition.

One common mode selection is obtained from the empirical POD (see, e.g. Holmes *et al.* 1998). It is optimal in the sense that it extracts the most energetic structures from a known flow solution. In the mathematical approach (Noack & Eckelmann 1994), completeness of the Galerkin expansion is guaranteed. The physical method (e.g. Rummler 2000) utilizes stability eigenmodes, thus economically describing linear behaviour.

An ordinary differential equation governing the Fourier coefficients $a_i(t)$ is obtained by substituting (5.1) into the Navier–Stokes equation (4.4) (actuation is not considered), and projecting onto the subspace spanned by the expansion modes:

$$(\mathscr{N}\,[\boldsymbol{u}(\boldsymbol{x},t)]\,,\boldsymbol{u}_i(\boldsymbol{x}))_\Omega=0\quad\text{for } i=1,\ldots,N. \tag{5.2}$$

The resulting Galerkin system is quadratically nonlinear

$$\frac{\mathrm{d}}{\mathrm{d}t}a_i=\nu\sum_{j=0}^{N}l_{ij}\,a_j+\sum_{j,k=0}^{N}q_{ijk}\,a_j\,a_k\quad\text{for } i=1,\ldots,N. \tag{5.3}$$

Table 1 provides the derivation of the coefficients l_{ij} and q_{ijk}. The contribution of the pressure term to the Galerkin system (last row in table 1) is neglected, since for absolutely unstable wake flows this term is relatively small (see, e.g. Noack, Papas & Monkewitz 2005). Alternatively, since the pressure term does not change the model structure, it can be lumped in the other coefficients.

In vector notation, the system reads

$$\frac{\mathrm{d}}{\mathrm{d}t}\boldsymbol{a}=\boldsymbol{c}+\boldsymbol{L}(\boldsymbol{a})+\boldsymbol{Q}(\boldsymbol{a},\boldsymbol{a}), \tag{5.4}$$

where we use the vector notations $\boldsymbol{a}\overset{\text{def}}{=}[a_1,\ldots,a_N]^T$, $\boldsymbol{c}\overset{\text{def}}{=}[c_1,\ldots,c_N]^T$ and

$$\boldsymbol{c}|_i\overset{\text{def}}{=}\nu l_{i0}+q_{i00},\qquad \boldsymbol{L}(\boldsymbol{a})|_i\overset{\text{def}}{=}\sum_{j=1}^{N}(\nu l_{ij}+q_{i0j}+q_{ij0})\,a_j,\qquad \boldsymbol{Q}(\boldsymbol{a},\boldsymbol{a})|_i\overset{\text{def}}{=}\sum_{j,k=1}^{N}q_{ijk}\,a_ja_k.$$

Truncation effects and numerical issues may result with substantial distortions of the predicted dynamics. Such distortions can be resolved by calibration methods (Galletti *et al.* 2004; Tadmor *et al.* 2004; Ausseur & Pinier 2005; Favier, Cordier & Kourta in press).

A Galerkin model of the boundary-actuated flow is challenging. A standard POD procedure slaves boundary unsteadiness with flow unsteadiness, i.e. boundary actuation is predicted by the dynamical system and cannot be imposed as actuation command. Most subdomain POD models fall in this category. Examples exist for the transitional boundary layer (Rempfer & Fasel 1994), the laminar and transitional

NSE	NSE with $\boldsymbol{u} = \boldsymbol{u}_0 + \boldsymbol{u}'$	Galerkin projection	Galerkin system	Simplified nomenclature
$\partial_t \boldsymbol{u} =$	$\partial_t \boldsymbol{u}' =$	$(\boldsymbol{u}_i, \partial_t \boldsymbol{u}')_\Omega =$	$\frac{\mathrm{d}}{\mathrm{d}t} a_i =$	$\frac{\mathrm{d}}{\mathrm{d}t} a_i =$
$-\nabla\cdot[\boldsymbol{u}\otimes\boldsymbol{u}]$	$-\nabla\cdot[\boldsymbol{u}_0\otimes\boldsymbol{u}_0]$	$-(\boldsymbol{u}_i, \nabla\cdot[\boldsymbol{u}_0\otimes\boldsymbol{u}_0])_\Omega$	q^c_{i00}	
	$-\nabla\cdot[\boldsymbol{u}'\otimes\boldsymbol{u}_0]$	$-(\boldsymbol{u}_i, \nabla\cdot[\boldsymbol{u}'\otimes\boldsymbol{u}_0])_\Omega$	$+\sum_{j=1}^{N} q^c_{ij0} a_j$	
	$-\nabla\cdot[\boldsymbol{u}_0\otimes\boldsymbol{u}']$	$-(\boldsymbol{u}_i, \nabla\cdot[\boldsymbol{u}_0\otimes\boldsymbol{u}'])_\Omega$	$+\sum_{j=1}^{N} q^c_{i0j} a_j$	
	$-\nabla\cdot[\boldsymbol{u}'\otimes\boldsymbol{u}']$	$-(\boldsymbol{u}_i, \nabla\cdot[\boldsymbol{u}'\otimes\boldsymbol{u}'])_\Omega$	$+\sum_{j,k=1}^{N} q^c_{ijk} a_j a_k$	$\sum_{j,k=0}^{N} q^c_{ijk} a_j a_k$
$+\nu\triangle\boldsymbol{u}$	$+\nu\triangle\boldsymbol{u}_0$	$+\nu\,(\boldsymbol{u}_i, \triangle\boldsymbol{u}_0)_\Omega$	$+\nu l_{i0}$	
	$+\nu\triangle\boldsymbol{u}'$	$+\nu\,(\boldsymbol{u}_i, \triangle\boldsymbol{u}')_\Omega$	$+\nu\sum_{j=1}^{N} l_{ij} a_j$	$+\nu\sum_{j=0}^{N} l_{ij} a_j$
$-\nabla p$	$-\nabla p_0$	$-(\boldsymbol{u}_i, \nabla p_0)_\Omega$	$+q^p_{i00}$	
	$-\nabla p'$	$-(\boldsymbol{u}_i, \nabla p')_\Omega$	$+\sum_{\substack{j,k=0 \\ j+k>0}}^{N} q^p_{ijk} a_j a_k$	$+\sum_{j,k=0}^{N} q^p_{ijk} a_j a_k$

TABLE 1. Derivation of the Galerkin system (GS). In each column the terms of the Navier–Stokes equation (NSE) are enlisted. The rows show the local acceleration, convective acceleration, viscous and pressure term. From left to right, the NSE is transformed into the GS in five steps: (i) NSE in its original form, (ii) NSE after Reynolds decomposition, (iii) Galerkin projection, (iv) GS and (v) a simplified nomenclature of the GS employing $a_0 \equiv 1$. The Galerkin projection of the pressure term is derived in Noack *et al.* (2005).

shear layer (Noack *et al.* 2005) and the turbulent mixing layer (Ukeiley *et al.* 2001; Noack *et al.* 2004*a*).

Boundary actuation is generally not derivable from the Galerkin projection, since this projection is explicitly designed to ignore boundary perturbations that are defined over a set of measure zero. However, on the Galerkin approximation level, boundary effects can be incorporated by additional *actuation modes* with imposed amplitudes. This technique has been employed in mathematical Galerkin models for decades (Ladyzhenskaya 1963; Hu *et al.* 1996). Recently, actuation modes have also been incorporated in the POD pendant, e.g. for wakes behind rotating and oscillating cylinders (Graham, Peraire & Tang 1999; Noack, Tadmor & Morzyński 2004*b*; Bergmann, Cordier & Brancher 2005) and for forced synthetic jets (Rediniotis, Ko & Kurdila 2002). The added control term in the Galerkin system (5.4) is state dependent and includes both the control command and its time derivative.

In the current discussion as in the generic case of periodic boundary actuation, the control command is restricted to be oscillatory with slowly varying periodic characteristics. In this case, the effect of forcing on the flow is often modelled by a forcing term $\boldsymbol{B}\,\boldsymbol{b}$ with actuation command $\boldsymbol{b}$, as, e.g. in Siegel, Cohen & McLaughlin (2003), Rowley & Juttijudata (2005); Samimy *et al.* (2007). Here, we follow this example and employ a constant matrix $\boldsymbol{B}$. As in (2.1), we focus on a periodic actuator where the velocity $b = B\cos(\beta)$ satisfies $\mathrm{d}\beta/\mathrm{d}t = \Omega^a$ with a slowly varying amplitude B and phase shift $\beta - \Omega^a t$. The acceleration reads $\mathrm{d}b/\mathrm{d}t = -\Omega^a B \sin(\beta)$. The

command and its derivative are comprised in

$$\boldsymbol{b} \stackrel{\text{def}}{=} \begin{bmatrix} b \\ -\dfrac{\mathrm{d}b/\mathrm{d}t}{\Omega^a} \end{bmatrix} = B \begin{bmatrix} \cos(\beta) \\ \sin(\beta) \end{bmatrix}. \tag{5.5}$$

This convention allows to identify time and phase shifts in the control vector. The resulting terms contain the most important subset of the forcing terms induced by the actuation mode (Noack *et al.* 2004*b*). In summary, the actuated Galerkin system reads

$$\frac{\mathrm{d}}{\mathrm{d}t}\boldsymbol{a} = \boldsymbol{c} + \boldsymbol{L}(\boldsymbol{a}) + \boldsymbol{Q}(\boldsymbol{a}, \boldsymbol{a}) + \boldsymbol{B}\,\boldsymbol{b}. \tag{5.6}$$

The physical justification of this form is given in § 7.3.

Following the literature, we assume that the same form can be employed for the URANS equations. Indeed, most POD models follow the URANS turbulence modelling philosophy by incorporating fine-scale fluctuations via one additional eddy viscosity (e.g. Aubry *et al.* 1988; Ukeiley *et al.* 2001), or via a modal eddy viscosity distribution (e.g. Rempfer & Fasel 1994; Couplet, Sagaut & Basdevant 2003). Some authors (e.g. Galletti *et al.* 2004) add a calibrated linear term. All these auxiliary models affect only the coefficients of the linear term $\boldsymbol{L}(\boldsymbol{a})$, not the very form of (5.6). The issue of turbulence modelling is re-visited in § 7.1.

5.2. *The least-order Galerkin approximation*

The least-order Galerkin approximation builds on the assumption NSE 1. We therefore look for modes which resolve the three flow contributions $\boldsymbol{u}^B$, $\boldsymbol{u}^n$ and $\boldsymbol{u}^a$ in (4.6). Optimal resolution of $\boldsymbol{u}^n$ and $\boldsymbol{u}^a$ over the natural and the actuated attractors, where these fluctuations are respectively most prominent, is achieved by POD expansions.

Indeed, let $\boldsymbol{u}_i^n$ and $\boldsymbol{u}_i^a$, $i = 1, 2$, be the dominant POD modes of these two attractors. We merge these four modes in an orthonormal basis $\{\boldsymbol{u}_i\}_{i=1}^4$ via Gram–Schmidt normalization, so that $\boldsymbol{u}_i = \boldsymbol{u}_i^n$, $\boldsymbol{u}_{i+2} = \boldsymbol{u}_i^a$, $i = 1, 2$. As seen in figure 6, the modes $\boldsymbol{u}_i^a$ reach peek fluctuation over and near the airfoil whereas the fluctuations represented by $\boldsymbol{u}_i^n$ are concentrated further downstream. This fact, along with the differences in the respective wavelengths imply that the two mode pairs are nearly orthogonal, to begin with, and the orthogonalization effect is minimal. We shall therefore maintain the association of the respective Fourier coefficient pairs with the natural and the actuated frequencies:

$$\boldsymbol{a}^n = a_1\,\boldsymbol{e}_1 + a_2\,\boldsymbol{e}_2, \quad \boldsymbol{a}^a = a_3\,\boldsymbol{e}_3 + a_4\,\boldsymbol{e}_4,$$

where $\boldsymbol{e}_i \stackrel{\text{def}}{=} [\delta_{i,1}, \ldots, \delta_{i,N}]^T$ is a unit vector in the ith direction and where we use the approximations

$$\boldsymbol{u}^n(\boldsymbol{x}, t) = \sum_{i=1}^{2} a_i(t)\,\boldsymbol{u}_i(\boldsymbol{x}), \quad \boldsymbol{u}^a(\boldsymbol{x}, t) = \sum_{i=3}^{4} a_i(t)\,\boldsymbol{u}_i(\boldsymbol{x}).$$

In Noack *et al.* (2003), the effect of the Reynolds stress due to the natural oscillations is represented by a *shift-mode* $\boldsymbol{u}_\Delta \propto \boldsymbol{u}_0^n - \boldsymbol{u}^s$, where $\boldsymbol{u}^s$ is the steady Navier–Stokes solution and $\boldsymbol{u}_0^n$ is the mean of the natural attractor. For later use, we introduce also the corresponding notation of the mean of the actuated attractor, $\boldsymbol{u}_0^a$. We shall follow this example and relate to an approximation of the time-varying base flow using two

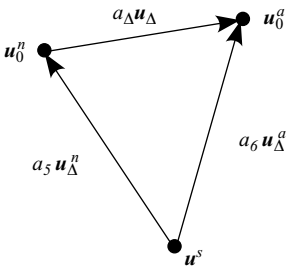

FIGURE 5. The relation between the steady solution and mean flows corresponding to the natural and actuated attractor. The steady solution $\boldsymbol{u}^s$ and the mean of the natural flow $\boldsymbol{u}_0^n$ and actuated pendant $\boldsymbol{u}_0^a$ are depicted as solid circles. The shift-modes $\boldsymbol{u}_\Delta^n$, $\boldsymbol{u}_\Delta^a$ are the vectors pointing from the steady solution to the natural and actuated mean flow, respectively. The normalized difference between the actuated and natural mean flows, denoted by $\boldsymbol{u}_\Delta$, corresponds to the shift-mode in figure 6(*b*).

shift-modes corresponding to the two attractors of interest,

$$\boldsymbol{u}^B(\boldsymbol{x}, t) = \boldsymbol{u}^s(\boldsymbol{x}) + \boldsymbol{u}^\Delta(\boldsymbol{x}, t) = \boldsymbol{u}^s(\boldsymbol{x}) + a_5(t)\, \boldsymbol{u}_5(\boldsymbol{x}) + a_6(t)\, \boldsymbol{u}_6(\boldsymbol{x}), \tag{5.7}$$

where $\{\boldsymbol{u}_i\}_{i=5}^6$ are derived by a Gram–Schmidt orthogonalization from $\boldsymbol{u}_\Delta^n \propto \boldsymbol{u}_0^n - \boldsymbol{u}^s$ and $\boldsymbol{u}_\Delta^a \propto \boldsymbol{u}_0^a - \boldsymbol{u}^s$, removing also any projection over $\{\boldsymbol{u}_i\}_{i=1}^4$. The Fourier coefficients of the two shift-modes are also collected in a column vector,

$$\boldsymbol{a}^B = a_5\, \boldsymbol{e}_5 + a_6\, \boldsymbol{e}_6.$$

The two mean flows $\boldsymbol{u}_0^n$ and $\boldsymbol{u}_0^a$ are approximated by the respective initial and terminal values of the time-varying base flow $\boldsymbol{u}^B$ trajectory in transients connecting the two attractors. Thus, the relevant linear approximation of the base flow is

$$\boldsymbol{u}^B(\boldsymbol{x}, t) = \boldsymbol{u}_0^n(\boldsymbol{x}) + a_\Delta(t)\, \boldsymbol{u}_\Delta(\boldsymbol{x}), \tag{5.8}$$

where $\boldsymbol{u}_\Delta \stackrel{\text{def}}{=} (\boldsymbol{u}_0^a - \boldsymbol{u}_0^n)/\|\boldsymbol{u}_0^a - \boldsymbol{u}_0^n\|_\Omega$. Figure 5 provides a schematic depiction of the resolution of the difference between the two mean flows.

The actual computation of $\{\boldsymbol{u}_i\}_{i=5}^6$ necessitates the difficult extraction of an unstable steady solution. In fact, we did not explicitly compute these modes. Invoking (5.8) instead of (5.7), the velocity field of the URANS data was approximated by the expression

$$\boldsymbol{u}(\boldsymbol{x}, t) = \boldsymbol{u}_0^n(\boldsymbol{x}) + a_\Delta(t)\, \boldsymbol{u}_\Delta(\boldsymbol{x}) + \sum_{i=1}^{4} a_i(t)\, \boldsymbol{u}_i(\boldsymbol{x}). \tag{5.9}$$

Nonetheless, expression (5.7) with both shift modes is still included in the formal Galerkin expansion that is used in the derivation of the Galerkin system, in § 5.3,

$$\boldsymbol{u}(\boldsymbol{x}, t) = \boldsymbol{u}^s(\boldsymbol{x}) + \sum_{i=1}^{6} a_i(t)\, \boldsymbol{u}_i(\boldsymbol{x}). \tag{5.10}$$

Since the Galerkin system coefficients will be obtained by a calibration method, using empirical data, the main purpose of (5.10) is to understand the implications on simplifying, special aspects of the structure of the Galerkin system, that will be utilized to facilitate system parameter estimation.

Decomposition (5.9) of the velocity field is schematically illustrated in figure 6. On the left, the mean of the natural and actuated flow, $\boldsymbol{u}_0^n$ and $\boldsymbol{u}_0^a$ respectively,

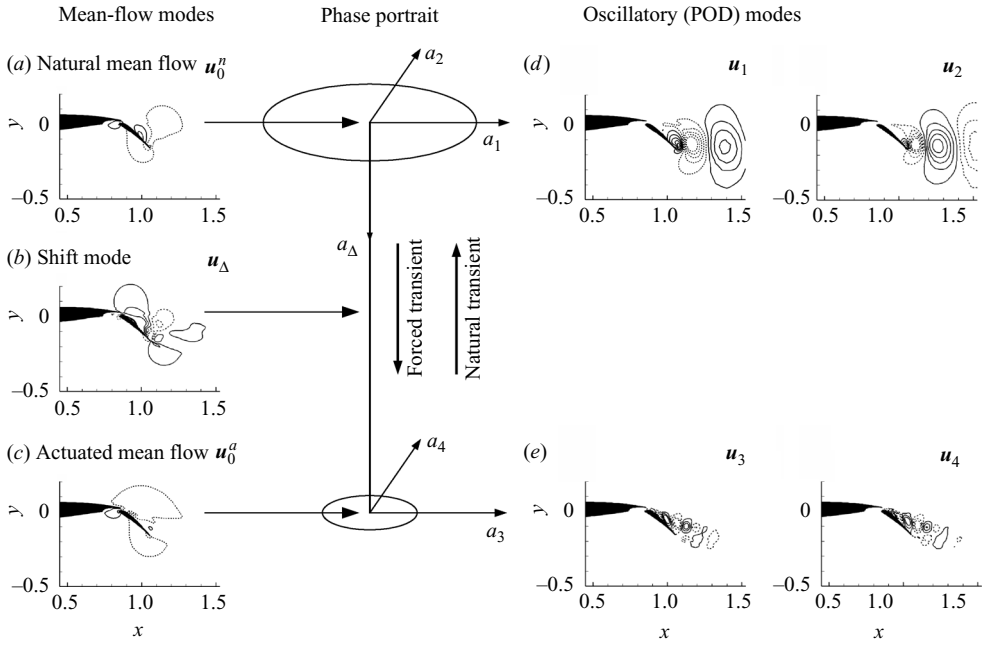

FIGURE 6. Principal sketch of the dynamics of a natural and actuated flow around a high-lift configuration. The flow is visualized by contour lines of the vertical velocity component, where continuous (dashed) lines indicate positive (negative) values. The depicted domain is the observation region indicated in figure 1. On the left, the mean fields of the natural (*a*) and actuated flow (*c*) are depicted. The shift-mode $\boldsymbol{u}_\Delta$ (*b*) is the normalized difference between them. On the right, the POD modes $\boldsymbol{u}_1$, $\boldsymbol{u}_2$ of the natural- (*d*) and of the actuated flow $\boldsymbol{u}_3$, $\boldsymbol{u}_4$ (*e*) are visualized. The middle column shows the phase portrait of the model, where the natural (actuated) attractor is depicted as the limit cycle spanned by a_1, a_2 (a_3, a_4). The actuated transient is from top to bottom and the natural transient vice versa.

along with the connecting (normalized) shift-mode $\boldsymbol{u}_\Delta \propto \boldsymbol{u}_0^n - \boldsymbol{u}_0^a$ is depicted. Modes representing the fluctuations are depicted on the right. Those include the first two POD modes of the natural and actuated attractor, $\boldsymbol{u}_{1,2}$ and $\boldsymbol{u}_{3,4}$, respectively. The phase portrait of the Fourier coefficients a_i is shown in the middle. A model based on this approximation accommodates the key physical phenomena of interest, including the natural and actuated limit cycles with their respective base flows, and transients between them. During an actuated transient, the coefficients representing the natural oscillator decay from their natural values to (near) zero at the actuated attractor, whereas the coefficients corresponding to the actuated oscillator grow from zero to their values on the actuated attractor.

5.3. *The least-order Galerkin system*

The least-order Galerkin system is obtained by substitution of the approximation (5.10) into the mean-field Navier–Stokes equations (4.9*b*, *c*) and (4.10), followed by a Galerkin projection of these equations on the expansion modes. Table 2 illustrates the derivation of the Galerkin system. In particular, we present the Galerkin system corresponding to the mean-field equation (4.9*b*) in table 2. The remaining four equations are derived in a similar fashion.

NSE (4.9*b*)	GS	
$\partial_t \boldsymbol{u}^n =$	$\frac{\mathrm{d}}{\mathrm{d}t} a_i =$	$i \in \mathscr{I}$
$-\nabla\cdot\left[\boldsymbol{u}^n \otimes \boldsymbol{u}^B\right]$	$\sum_{j\in\mathscr{I}}\sum_{k\in\mathscr{K}} q_{ijk} a_j a_k$	
$-\nabla\cdot\left[\boldsymbol{u}^B \otimes \boldsymbol{u}^n\right]$	$+\sum_{j\in\mathscr{K}}\sum_{k\in\mathscr{I}} q_{ijk} a_j a_k$	
$+\nu\triangle\boldsymbol{u}^n$	$+\nu\sum_{j=1}^{2} l_{ij} a_j$	
$-\nabla p^n$	$+0$	

TABLE 2. Projection of the mean-field Navier–Stokes equation (4.9*b*) (NSE) to form the Galerkin system (GS) using the least-order approximation (5.10). In the first column the terms of the NSE are provided and in the second one the corresponding GS counterparts. The employed index sets are $\mathscr{I} = \{1, 2\}$ and $\mathscr{K} = \{5, 6\}$.

The complete Galerkin system can be summarized in vector notation,

$$\frac{\mathrm{d}}{\mathrm{d}t}\boldsymbol{a}^n = \boldsymbol{L}(\boldsymbol{a}^n) + \boldsymbol{Q}(\boldsymbol{a}^B, \boldsymbol{a}^n) + \boldsymbol{Q}(\boldsymbol{a}^n, \boldsymbol{a}^B), \tag{5.11a}$$

$$\frac{\mathrm{d}}{\mathrm{d}t}\boldsymbol{a}^a = \boldsymbol{L}(\boldsymbol{a}^a) + \boldsymbol{Q}(\boldsymbol{a}^B, \boldsymbol{a}^a) + \boldsymbol{Q}(\boldsymbol{a}^a, \boldsymbol{a}^B) + \boldsymbol{B}\,\boldsymbol{b}, \tag{5.11b}$$

$$0 = \boldsymbol{L}(\boldsymbol{a}^B) + \overline{\boldsymbol{Q}(\boldsymbol{a}^n, \boldsymbol{a}^n)} + \overline{\boldsymbol{Q}(\boldsymbol{a}^a, \boldsymbol{a}^a)}. \tag{5.11c}$$

Here, we slightly abuse notations, identifying $\boldsymbol{a}^n$ and $\boldsymbol{a}^a$ with the respective $\Re^2$ vectors $[a_1, a_2]^T$ and $[a_3, a_4]^T$. The notational polymorphism extends to the matrix coefficients: in (5.6), $\boldsymbol{B}$ represents a 6×2 matrix whereas in (5.11*b*) the same notation denotes the non-vanishing 2×2 sub-matrix.

In Appendix B we show that under the current assumptions and the assumption of phase invariance (NSE 3) the mean-field Galerkin system has the following structure:

$$\frac{\mathrm{d}}{\mathrm{d}t}\begin{bmatrix} a_1 \\ a_2 \\ a_3 \\ a_4 \end{bmatrix} = \begin{bmatrix} \tilde{\sigma}^n & -\tilde{\omega}^n & 0 & 0 \\ \tilde{\omega}^n & \tilde{\sigma}^n & 0 & 0 \\ 0 & 0 & \tilde{\sigma}^a & -\tilde{\omega}^a \\ 0 & 0 & \tilde{\omega}^a & \tilde{\sigma}^a \end{bmatrix} \begin{bmatrix} a_1 \\ a_2 \\ a_3 \\ a_4 \end{bmatrix} + \begin{bmatrix} 0 & 0 \\ 0 & 0 \\ \kappa & -\lambda \\ \lambda & \kappa \end{bmatrix} \boldsymbol{b}, \tag{5.12}$$

where the state-dependent coefficients are of the form

$$\begin{aligned} \tilde{\sigma}^n &= \sigma^n - \sigma^{n,n}\,(A^n)^2 - \sigma^{n,a}\,(A^a)^2, \\ \tilde{\omega}^n &= \omega^n + \omega^{n,n}\,(A^n)^2 + \omega^{n,a}\,(A^a)^2, \\ \tilde{\sigma}^a &= \sigma^a - \sigma^{a,n}\,(A^n)^2 - \sigma^{a,a}\,(A^a)^2, \\ \tilde{\omega}^a &= \omega^a + \omega^{a,n}\,(A^n)^2 + \omega^{a,a}\,(A^a)^2, \end{aligned} \tag{5.13}$$

and $A^n \overset{\text{def}}{=} \|\boldsymbol{a}^n\|$ and $A^a \overset{\text{def}}{=} \|\boldsymbol{a}^a\|$ are the respective oscillation amplitudes. Without the linearization assumption NSE 4, the parameters are represented by a Taylor series in $(A^n)^2$ and $(A^a)^2$.

5.4. *Discussion of the dynamical system*

In this section, dynamical system (5.12) is analysed in more detail. The assumed phase invariance and lock-in of the actuation response enable a notational simplification of

the system by transforming to polar coordinates. The discussion leads to algebraic constraints of the system parameters. In addition, we further simplify the dynamical system.

The natural fluctuation $\boldsymbol{a}^n$ is characterized by the amplitude A^n and phase α^n. Similarly, polar coordinates of the forced fluctuation $\boldsymbol{a}^a$ are the amplitude A^a and phase α^a. Thus,

$$\begin{aligned} \boldsymbol{a}^n &= A^n\,[\cos(\alpha^n)\,\boldsymbol{e}_1 + \sin(\alpha^n)\,\boldsymbol{e}_2], \\ \boldsymbol{a}^a &= A^a\,[\cos(\alpha^a)\,\boldsymbol{e}_3 + \sin(\alpha^a)\,\boldsymbol{e}_4]. \end{aligned} \tag{5.14}$$

The control command (5.5) acts in the evolution equation (5.6) only on the forced fluctuation. Hence,

$$\boldsymbol{b} = B\,[\cos(\beta)\,\boldsymbol{e}_3 + \sin(\beta)\,\boldsymbol{e}_4].$$

Finally, by Observation B.3 in the Appendix, the matrix coefficient $\boldsymbol{B}$ can be written in the form

$$\boldsymbol{B} = g \begin{bmatrix} \cos(\theta) & -\sin(\theta) \\ \sin(\theta) & \cos(\theta) \end{bmatrix}. \tag{5.15}$$

Using these notations, we rewrite (5.12) as

$$\frac{\mathrm{d}A^n}{\mathrm{d}t} = \tilde{\sigma}^n A^n, \tag{5.16a}$$

$$\frac{\mathrm{d}\alpha^n}{\mathrm{d}t} = \tilde{\omega}^n, \tag{5.16b}$$

$$\frac{\mathrm{d}A^a}{\mathrm{d}t} = \tilde{\sigma}^a A^a + gB\cos(\beta + \theta - \alpha^a), \tag{5.16c}$$

$$\frac{\mathrm{d}\alpha^a}{\mathrm{d}t} = \tilde{\omega}^a + \frac{gB}{A^a}\sin(\beta + \theta - \alpha^a), \tag{5.16d}$$

where we refer to the state dependencies of $\tilde{\sigma}^n$, $\tilde{\sigma}^a$, $\tilde{\omega}^n$ and $\tilde{\omega}^a$, as defined in (5.13).

On the two attractors, the time derivatives of the amplitudes in (5.16*a*) and (5.16*c*) must vanish, and the right-hand side terms of (5.16*b*) and (5.16*d*) must be equal to the respective steady-state shedding frequency and the actuation frequency. In deriving these equations, we denote by $A^{n,n}$ (respectively $A^{a,a}$) the steady-state value of A^n on the natural (respectively actuated) attractor. According to assumption NSE 1, the natural harmonic vanishes under forcing and the actuation harmonic vanishes without forcing. Hence, the values of A^n on the actuated attractor and of A^a on the natural attractor are set to zero.

The converged amplitudes on the natural and the actuated attractor, i.e. $\mathrm{d}A^n/\mathrm{d}t = 0$ and $\mathrm{d}A^a/\mathrm{d}t = 0$, respectively, lead to the following equations:

$$0 = \sigma^n - \sigma^{n,n}\,(A^{n,n})^2\,, \tag{5.17a}$$

$$0 = (\sigma^a - \sigma^{a,a}(A^{a,a})^2)A^{a,a} + gB\cos(\beta + \theta - \alpha^a). \tag{5.17b}$$

The lock-in property implies $\mathrm{d}\alpha^a/\mathrm{d}t = \mathrm{d}\beta/\mathrm{d}t = \Omega^a$ on the actuated attractor. Thus, $\beta + \theta - \alpha^a$ is constant in (5.17*b*) and (5.18*b*). We shall re-visit this term shortly.

The constant frequency conditions yield

$$\Omega^n = \tilde{\omega}^{n,n}, \tag{5.18a}$$

$$\Omega^a = \tilde{\omega}^{a,a} + \frac{gB}{A^{a,a}}\sin(\beta + \theta - \alpha^a), \tag{5.18b}$$

where again, the notation $\tilde{\omega}^{n,n}$ stands for the steady-state value of $\tilde{\omega}^n$ on the natural attractor and $\tilde{\omega}^{a,a}$ for the actuated attractor value of $\tilde{\omega}^a$.

Equation (5.18*b*) is simplified by assuming that the oscillation frequencies are independent of A^a and A^n and that the flow locks in with the actuation frequency ω^a. In other words, the coefficients describing amplitude-dependent frequency changes vanish:

$$\omega^{n,n} = \omega^{n,a} = \omega^{a,a} = \omega^{a,n} = 0. \tag{5.19}$$

The approximation $\omega^{n,n} = \omega^{n,a} = 0$ appears admissible for the vortex-shedding frequency from dead-water zones with well-defined transverse extent. Typically, frequency changes are at most of the order of 10%. Equation $\omega^{a,n} = \omega^{a,a} = 0$ is implied by the assumed lock-in. Thus, we have

$$\tilde{\omega}^n = \omega^n = \Omega^n, \tag{5.20a}$$

$$\tilde{\omega}^a = \omega^a = \Omega^a, \tag{5.20b}$$

$$\theta = \alpha^a - \beta. \tag{5.20c}$$

In particular, $\cos(\beta + \theta - \alpha^a) = 1$ on the actuated attractor, hence in (5.17*b*).

5.5. *Parameter identification*

The parameters of the least-order model are identified by calibration with simulation data. We chose to use for that purpose a data trajectory that involves step changes in the actuation, as described in § 6. That reference was selected as a generic example of open-loop actuation. It is noted that abrupt transients present an inherent challenge for low-order models, due to the fact that they tend to involve far richer dynamics than what can ideally be represented, say, by a mere single mode pair per frequency. In particular, transient data has limited value to the calibration procedure, necessitating some added simplification in the model, as discussed in the previous section (5.19). In view of this, the success demonstrated in § 6 illustrates the robustness of the proposed modelling concept, corroborating its fundamental underpinning in the physics of the system.

System (5.16), with state-dependent coefficients given by (5.13), contains 14 unknown parameters: σ^n, $\sigma^{n,n}$, $\sigma^{n,a}$, ω^n, $\omega^{n,n}$, $\omega^{n,a}$, σ^a, $\sigma^{a,n}$, $\sigma^{a,a}$, ω^a, $\omega^{a,n}$, $\omega^{a,a}$, g and θ. Using the results of the previous section, (5.17), (5.19) and (5.20), this number reduces to seven. These remaining degrees of freedom (σ^n, $\sigma^{n,n}$, $\sigma^{n,a}$, σ^a, $\sigma^{a,n}$, $\sigma^{a,a}$, g) are estimated from (5.16), using transient amplitude data. Specifically, the parameters are selected as the solutions of the following least-mean square problems

$$\min \int_{t_0}^{t_1} \mathrm{d}t \left[\frac{\mathrm{d}A^n}{\mathrm{d}t} - \tilde{\sigma}^n A^n\right]^2, \tag{5.21a}$$

$$\min \int_{t_0}^{t_1} \mathrm{d}t \left[\frac{\mathrm{d}A^a}{\mathrm{d}t} - \tilde{\sigma}^a A^a - g B \cos(\beta + \theta - \alpha^a)\right]^2, \tag{5.21b}$$

subject to the algebraic constraints (5.17).

In summary, the algorithm for determining the parameters of the least-order Galerkin system is as follows:

(*a*) *Natural frequency* (ω^n, $\omega^{n,n}$, $\omega^{n,a}$): The parameters are algebraically determined by (5.19) and (5.20*a*).

(*b*) *Actuated frequency* (ω^a, $\omega^{a,n}$, $\omega^{a,a}$): These parameters are determined by (5.19) and (5.20*b*).

(iii) *Growth-rate of the fluctuation at natural frequency* (σ^n, $\sigma^{n,n}$, $\sigma^{n,a}$): The coefficients determining the growth rate $\tilde{\sigma}^n$ are constrained by (5.17*a*). This constraint

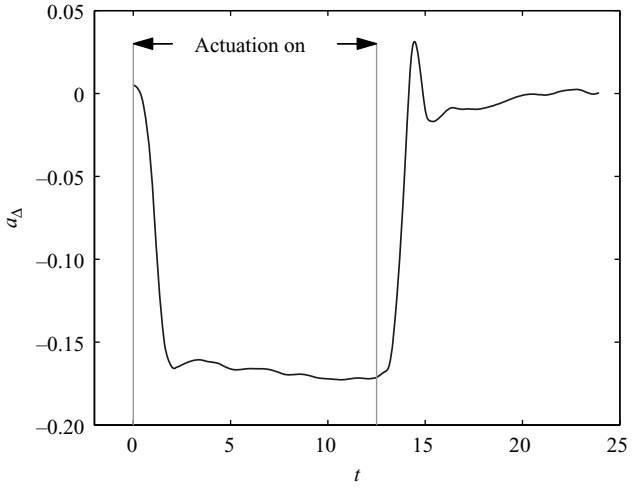

FIGURE 7. The shift-mode amplitude a_Δ as obtained from Galerkin projection of the URANS data. Actuation is switched on at $t = 0$ and is switched off at $t = 12.5$.

is used to express $\tilde{\sigma}^n$ in terms of σ^n and $\sigma^{n,a}$, i.e. $\tilde{\sigma}^n(\sigma^n, \sigma^{n,a})$. A transient part of the trajectory is used to determine σ^n and $\sigma^{n,a}$ by a least-mean-square fit (5.21*a*).

(iv) *Growth-rate of the fluctuation at the actuated frequency* (σ^a, $\sigma^{a,n}$, $\sigma^{a,a}$) *and actuation gain* (g)*:* The coefficients determining the growth rate $\tilde{\sigma}_a$ and the gain g are constrained by (5.17*b*). The expression for the rate is simplified to $\tilde{\sigma}^a = \sigma^a$, i.e. $\sigma^{a,n} = \sigma^{a,a} = 0$. Note that the lock-in assumption implies a fixed phase difference $\theta = \alpha^a - \beta$. Hence, the control term is zero without actuation and $g\,B$ under actuation. This means that constraint (5.17*b*) simplifies to $0 = \sigma^a + g\,B$. This constraint is used to express $\tilde{\sigma}^n$ in terms of σ^a. A transient part of the trajectory is used to determine σ^a, by a least square fit (5.21*b*).

6. Comparison of the Galerkin model with URANS simulation

The Galerkin model derived in § 5 is compared with the empirical data from a transient URANS simulation. This comparison includes the Galerkin approximation of the flow field (§ 6.1), the Galerkin system for the dynamics (§ 6.2) and the lift coefficient (§ 6.3).

6.1. *Galerkin approximation of the transient simulation*

Here, the transient URANS data are analysed. The snapshots of the velocity field are Galerkin approximated as in (5.8) and (5.10). The shift-mode amplitude a_Δ is shown in figure 7. The amplitude indicates how the mean flow changes from the value at the natural attractor. As actuation is turned on, the mean flow changes and settles at the actuated attractor. At the same time the Fourier coefficients a_1 and a_2, corresponding to the first oscillator, decrease to near-zero at the actuated attractor (see figure 8*a*). The coefficients of the second oscillator, a_3 and a_4, are excited by the periodic actuation (see figures 8*a* and 8*b*). If actuation is turned off, the roles of both coefficient pairs are reversed. This behaviour is also elucidated in the principal sketch in figure 6.

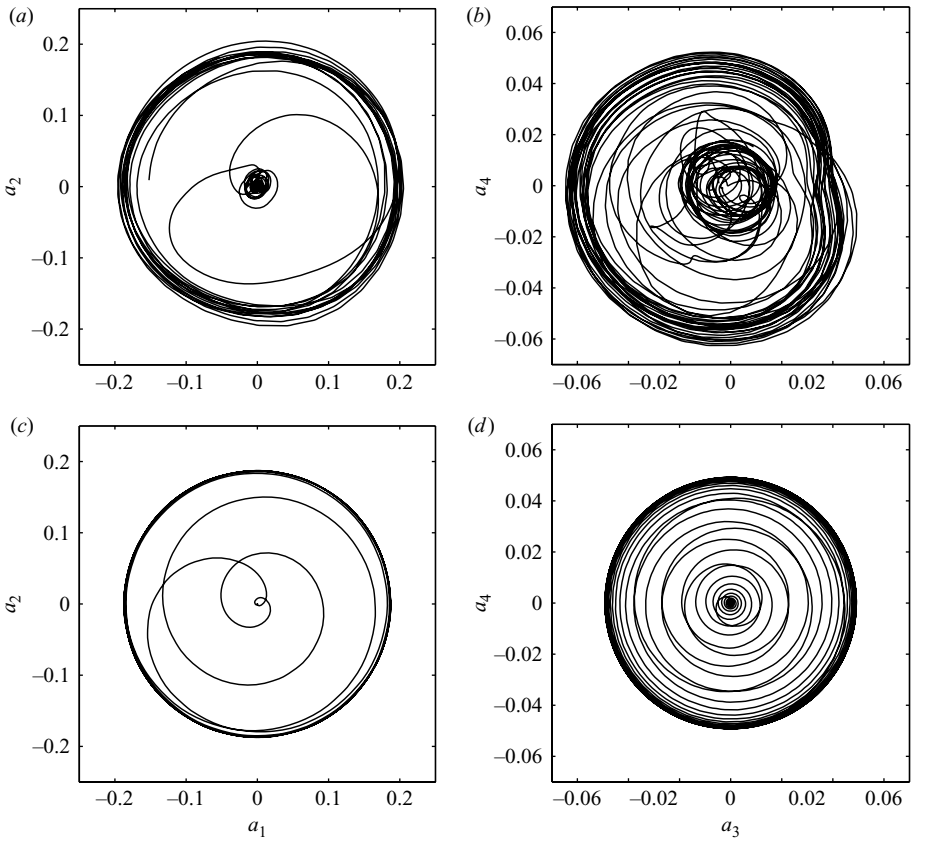

FIGURE 8. Phase portraits of the URANS simulation (*a*,*b*) and the least-order Galerkin model (*c*,*d*). The left column (*a*,*c*) shows the trajectory (a_1, a_2), the right (*b*,*d*) shows the trajectory (a_3, a_4) associated with the natural and actuated flow.

6.2. *Least-order Galerkin model of the transient data*

In this section, the URANS data are compared with the least-order Galerkin model prediction (5.16). The Fourier coefficients that result from projection onto the Galerkin expansion are used as a database for the calibration. The values of the model parameters are given in table 3. These parameters yield growth and decay rates in (5.12) that are bounded at $|\tilde{\sigma}^n| < 10$ and $|\tilde{\sigma}^a| < 1$. An order of magnitude estimation using (5.16*a*), which has an exponential solution at a fixed instant in time, shows that the decay rate must be large to describe the steep descent, thus explaining the high values in table 3. These values of the rate coefficients in the table are due the fast convection of the structures in the observation region (see figure 1) and the short transients.

The phase portraits as predicted by time integration of the least-order Galerkin model are shown in figures 8(*c*) and 8(*d*) and can be compared with the projected values from the URANS simulation in the first row of figure 8. A comparison of the behaviour of the low-pass filtered amplitudes A^n and A^a from URANS data and integration of (5.16) are shown in figure 9. A good agreement is achieved. However, the natural attractor of the URANS simulation has a small residual level in A^a relative to A^n. According to our assumption NSE 1, the actuation harmonic vanishes without forcing. Hence, this level vanishes in the model.

	Parameter	Value
Linear dynamics	ω^n	7.92
	ω^a	14.85
	σ^n	10.00
	σ^a	−0.80
Mean-field effects	$\sigma^{n,n}$	286.0
	$\sigma^{n,a}$	8243.0
	$\omega^{n,n}$	0.0
	$\omega^{n,a}$	0.0
	$\sigma^{a,n}$	0.0
	$\sigma^{a,a}$	0.0
	$\omega^{a,n}$	0.0
	$\omega^{a,a}$	0.0
actuation	g	2.06×10^{-2}
	θ	−3.69

TABLE 3. Identified parameters for the generalized mean-field model (see (5.16)). The actuation amplitude $B = 1.91$ is determined by the URANS configuration.

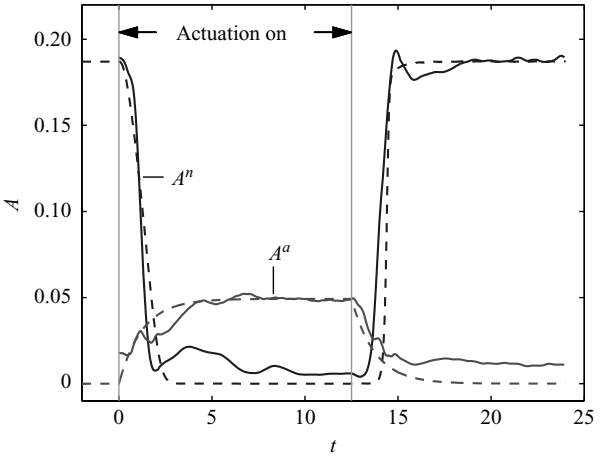

FIGURE 9. The amplitudes A^n and A^a of the URANS data (continuous lines) and the predictions by the least-order Galerkin model (dashed lines) in dependency of the time. Actuation is switched on at $t = 0$ and is switched off at $t = 12.5$. The URANS values are low-pass filtered.

From figure 6, it can be seen that the dominant natural harmonic is mainly present after the flap in a large separation zone, whereas the actuated mode is active in a smaller region starting at the leading edge of the flap. The modes thus act as rivals, where only one can be fully alive in its own space.

Particularly important for flow control is the phase prediction by the model. The approximate lock-in on the actuated attractor is shown for Fourier coefficient a_3 in figure 10.

6.3. *Estimation of the lift coefficient*

The model predictions can be related to quantities of engineering interest. As an example, we show the prediction of the lift coefficient by the model. The lift coefficient

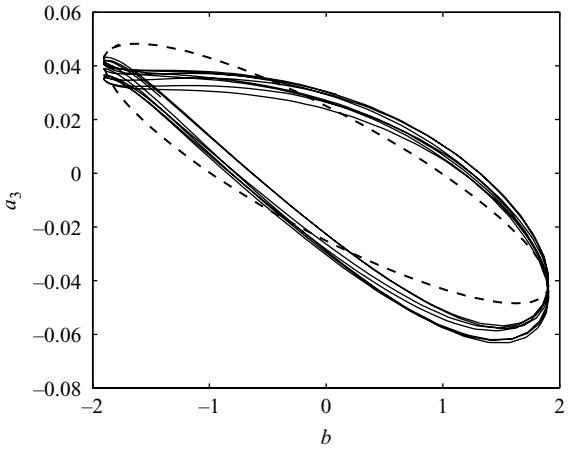

FIGURE 10. A phase portrait of the forced dynamics. Fourier coefficient a_3 versus the actuation command $b = B\cos(\beta)$. The URANS data is shown by a continuous line and the least-order Galerkin model prediction by a dashed line. The approximate lock-in of URANS to the forcing frequency is clearly visible.

will be inferred from the reduced-order model in two ways. Following the overall pattern of this section, we provide here a calibrated polynomial expression based on the least-order Galerkin model. In § 7.4, we briefly outline an analytic approximation using the definition of the lift coefficient, and compare its prediction with both the least-order model and the actual lift coefficient.

We assume that the lift coefficient is function of the Fourier coefficients $c_l(a_1, \ldots, a_4)$. The oscillatory behaviour of the lift coefficient is modelled by a linear combination of a_1, a_2, a_3 and a_4. The influence of the mean-field deformation during transients is taken into account by a Taylor series of second order in $(A^n)^2$ and $(A^a)^2$ (see (5.11*c*)).

Thus, the measurement equation for the lift coefficient is assumed to be of the following form:

$$c_l(t) = c_{l0} + \sum_{i=1}^{4} k_i\, a_i(t) + k_5(A^n)^2 + k_6(A^a)^2 + k_7(A^n)^4 + k_8(A^a)^4. \tag{6.1}$$

The first part of the functional form, up to the quadratic terms, follows directly from the Navier–Stokes equation. The two remaining fourth-order terms are conjectured to account for unmodelled mode deformations. The parameters $k_1, \ldots, k_8$ obtained from a least-squares fit from natural and actuated transients are listed in table 4.

The result is shown in figure 11, where the original lift coefficient is compared with the prediction of the model. The least-order Galerkin model performs surprisingly well. Prediction during fast transients (particularly, the second one) requires a more accurate dynamical model.

7. Discussion

In this section, we address Galerkin modelling aspects related to the pursued structure and parameter identification for turbulent flows represented by URANS data. In principle, the model should be derivable from the Navier–Stokes equation from accurate DNS data. In practice, only URANS or PIV data may be available for turbulent flows and the mean-field considerations as well as the parameter

	Parameter	Value
	c_{l0}	2.05
Linear dynamics	k_1	0.15
	k_2	−0.55
	k_3	−0.47
	k_4	0.70
	k_5	15.19
Mean-field effects	k_6	212.31
	k_7	−436.00
	k_8	-3.75×10^4

TABLE 4. Identified parameters of the measurement equation for the lift coefficient (see (6.1)).

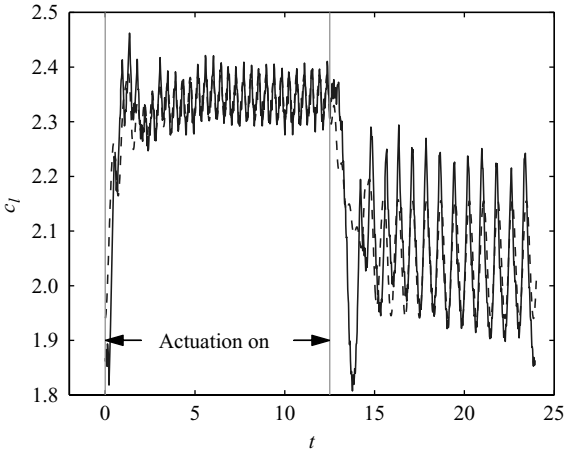

FIGURE 11. The original lift coefficient (continuous line) compared with the reconstructed lift coefficient (dashed line) based on the least-order Galerkin model. Actuation is switched on at $t = 0$ and is switched off at $t = 12.5$.

identification require a more rigorous justification. These modelling aspects include effects of turbulence (§ 7.1), of non-equilibrium (§ 7.2) and of actuation (§ 7.3). In § 7.4, the lift formula is derived from first principles and compared with the identified formula.

7.1. *Turbulence effects*

The rational of URANS simulations is that large-scale coherent structures are resolved in space and time while small-scale fluctuations are modelled via an eddy viscosity ansatz. This implies that the generalized Krylov–Bogoliubov approximation (4.6) should be augmented with a term $\boldsymbol{u}^t$ representing the contribution of small-scale dynamics:

$$\boldsymbol{u}(\boldsymbol{x}, t) = \boldsymbol{u}^B(\boldsymbol{x}, t) + \boldsymbol{u}^n(\boldsymbol{x}, t) + \boldsymbol{u}^a(\boldsymbol{x}, t) + \boldsymbol{u}^t(\boldsymbol{x}, t). \tag{7.1}$$

Small-scale fluctuations are characterized by high-frequency behaviour which can be expected to be uncorrelated with the large-scale coherent structures. Assuming that to be the case, $\boldsymbol{u}^t$ and products with it vanish under ensemble averaging and low-pass filtering. In particular, the filtered Navier–Stokes equations, like (4.9) and

its derivations, are not effected by $\boldsymbol{u}^t$. This small-scale fluctuation is the difference between an accurate DNS and ideal URANS simulation.

However, $\boldsymbol{u}^t$ acts as an energy sink in the evolution equations. In URANS and LES an eddy viscosity accounts for these losses. In POD Galerkin models, Rempfer & Fasel (1994) proposed modal eddy viscosities $\nu_{T,i}$ to account for that effect – in analogy to spectral pendants:

$$\dot{a}_i = (\nu + \nu_{T,i}) \sum_{j=0}^{N} l_{ij} a_j + \sum_{j,k=0}^{N} q_{ijk}\, a_j\, a_k. \tag{7.2}$$

The eddy viscosity has a negligible effect on frequencies since l_{ij} is a diagonal matrix in good approximation.

A comparison of the Galerkin projected system and the identified system, at the natural and actuated attractor, shows that the frequencies of both systems are similar. In contrast, the growth rates are not predicted correctly by the Galerkin projection. This is due to the neglected effect of turbulence, as described above.

In summary, neglecting the small-scale fluctuation is standard in reduced-order models. This is expected neither to change the mean-field equations nor the derived structure of the least-order Galerkin system. The effect of this simplification is mostly restricted to growth rates, which can be corrected by careful calibration. This seems to be an acceptable price for the level of simplicity and physical insight associated with the reduced-order model. In particular, a minimum number of free parameters makes this approach particularly suited for the evaluation of experimental PIV data.

7.2. *Non-equilibrium effects*

The steady solution is critical for the derivation of the standard and the presented generalized mean-field model. More specifically, the two shift modes that govern the nonlinear fluctuation growth rates are defined as the unit vectors pointing from the steady solution to the respective mean flows of the natural and the actuated attractors.

Thus, the knowledge of the steady solution is necessary for the derivation of the dynamical model from the Navier–Stokes equation. However, this unstable solution cannot be obtained from the URANS solver. Fortunately, the parameters governing the dynamical model can be estimated from URANS transient data (see § 5.5), and the steady solution as well as the shift modes are not needed. In a similar spirit, experimentalists have determined the constants of the Landau equation for the onset of vortex shedding without inquiring the Navier–Stokes equation.

Equation (5.8) serves as an auxiliary model to the mean-field system (5.12), where a_Δ could be obtained as a fitted polynomial of the oscillation amplitudes A^n and A^a. Similarly, the lift coefficient (6.1) is embedded in the model by a fitted polynomial of the modal coefficients $a_1, \ldots, a_4$ and the oscillation amplitudes.

7.3. *Actuation effects*

In this section, the actuation model is re-considered. The effect of the zero-net-mass-flux actuator was represented by an equivalent volume force term. In the first principles treatment, this effect can be resolved by an additional actuation mode $\boldsymbol{u}_{-1}(\boldsymbol{x})$ with amplitude $a_{-1}(t)$ (see, e.g. Graham *et al.* 1999). This results in the Galerkin approximation

$$\boldsymbol{u}(\boldsymbol{x}, t) = \sum_{i=-1}^{N} a_i(t)\, \boldsymbol{u}_i(\boldsymbol{x}). \tag{7.3}$$

The choice of the actuation mode is a free design parameter, for which the literature offers many variants. Here, we shall only be concerned whether the postulated surrogate volume force term is consistent with an actuation mode ansatz under nearly periodic forcing. The actuation mode has two particularities: firstly, it is not necessarily orthogonal to the POD modes, and secondly, its amplitude is a control input. We can identify $b_1 = a_{-1}$ and $b_2 = \dot{a}_{-1}/\omega^a$ in (5.5). Galerkin projection of (7.3) onto the Navier–Stokes equation yields (Noack *et al.* 2004*c*)

$$\dot{a}_i = -m_{i,-1}\,\dot{a}_{-1} + \nu \sum_{j=-1}^{N} l_{ij}\,a_j + \sum_{j,k=-1}^{N} q_{ijk}\,a_j\,a_k \quad \text{for } i = 1, \ldots, N.$$

or, equivalently,

$$\begin{aligned}\dot{a}_i = {} & \nu \sum_{j=0}^{N} l_{ij}\,a_j + \sum_{j,k=0}^{N} q_{ijk}\,a_j\,a_k \\ & + \left[\nu\, l_{i,-1} + (q_{i,0,-1} + q_{i,-1,0}) + \sum_{j=1}^{N} (q_{i,j,-1} + q_{i,-1,j})\,a_j\right] b_1 \\ & - m_{i,-1}\,\omega^a b_2. \end{aligned} \tag{7.4}$$

Under non-actuated conditions, $b_1 = b_2 \equiv 0$, and (7.4) is equivalent to (5.3). Under periodic forcing, $a_1 = a_2 \equiv 0$, a_5, a_6 are constant and a_3, a_4, b_1 and b_2 are locked-in at the same frequency ω^a. In this case (7.4) can be approximated by

$$\dot{a}_i = \nu \sum_{j=0}^{N} l_{ij}\,a_j + \sum_{j,k=0}^{N} q_{ijk}\,a_j\,a_k + B_{i1}b_1 + B_{i2}b_2 \tag{7.5}$$

neglecting higher harmonics. Here, B_{i1} and B_{i2} can be easily derived from (7.4). Equation (7.5) can be derived under more general Krylov–Bogoliubov assumptions. Note that (7.5) is equivalent to (5.6) and thus justifies the volume force ansatz.

7.4. *Lift formula*

In this section, a formula for the lift coefficient is derived in terms of the Fourier coefficients from the Navier–Stokes equation. The result of this analytical formula is compared with the calibrated lift coefficient in § 6.3.

The lift coefficient comprises a pressure and viscous contribution:

$$c_l = \frac{1}{1/2\rho(U_\infty)^2 c}\left(-\int_\Gamma p\boldsymbol{n}\,\mathrm{d}S + \nu\int_\Gamma \nabla\boldsymbol{u}\cdot\boldsymbol{n}\,\mathrm{d}S\right)\cdot\boldsymbol{e}_y, \tag{7.6}$$

where Γ is the contour of the high-lift configuration, $\boldsymbol{n}$ the outward normal vector and $\boldsymbol{e}_y$ defines the direction of the lift.

The viscous contribution can easily be expressed in terms of the Fourier coefficients by substituting the Galerkin approximation (5.1) in (7.6). The pressure field p is expanded into N modes p_i which are obtained from the M pressure snapshots p^m in complete analogy to the corresponding velocity snapshots $\boldsymbol{u}^m$ at the same times. More specifically, let $\boldsymbol{u}_i = \sum_{m=1}^{M} \boldsymbol{T}_i^m \boldsymbol{u}^m$ be the formula of the POD snapshot method with the transformation matrix $\boldsymbol{T}_i^m$ of the observation region in figure 1. Then, $p_i = \sum_{m=1}^{M} \boldsymbol{T}_i^m p^m$. Physically, this corresponds exactly to the empirical pressure model of Noack *et al.* (2005), which is found to be a good approximation for all considered free shear flows, including shear-layers and wakes (Noack 2006). The

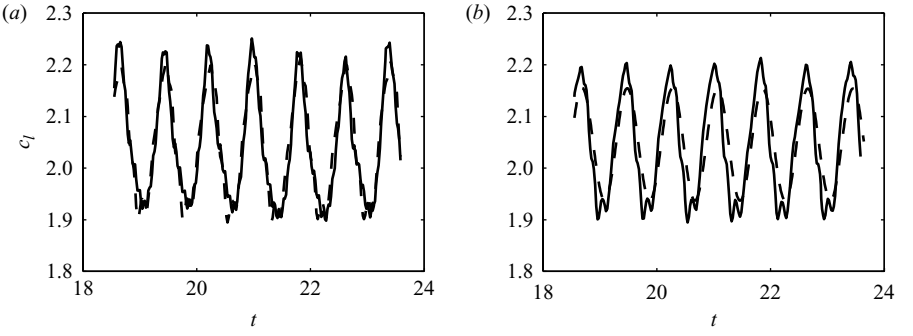

FIGURE 12. Comparison of the actual, modal and identified lift coefficient at the natural attractor: (*a*) actual (continuous line) and modal lift coefficient (dashed line), (*b*) modal (continuous line) and identified lift coefficient (dashed line).

resulting expansions of the flow variables read

$$\boldsymbol{u}(\boldsymbol{x}, t) = \sum_{i=0}^{N} a_i(t)\, \boldsymbol{u}_i(\boldsymbol{x}), \tag{7.7a}$$

$$p(\boldsymbol{x}, t) = \sum_{i=0}^{N} a_i^p(t)\, p_i(\boldsymbol{x}), \tag{7.7b}$$

where $a_0 \equiv 1$ and $a_0^p \equiv 1$ by definition. Thus, the lift coefficient can be written as

$$c_l(t) = \frac{1}{1/2\rho(U_\infty)^2 c} \sum_{i=0}^{N} \left\{ -\left(\int_\Gamma p_i(\boldsymbol{x}) \boldsymbol{n} \mathrm{d}S \right) a_i^p(t) + \nu \left(\int_\Gamma \nabla \boldsymbol{u}_i(\boldsymbol{x}) \cdot \boldsymbol{n} \mathrm{d}S \right) a_i(t) \right\} \cdot \boldsymbol{e}_y. \tag{7.8}$$

We compute the modal lift coefficient for $N = 2$ at the natural attractor. The comparison of the actual and modally decomposed lift coefficient is shown in figure 12(*a*). A good agreement is achieved with only two modes. Figure 12(*b*) shows the comparison of the modal and identified lift coefficient (see also figure 11). It can be seen that the identified lift coefficient is smoother than the modal one. This observation directly correlates with the temporal amplitudes of the velocity field, which are much smoother than the amplitudes of the pressure modes. The latter correlate better with the lift coefficient. The identified lift coefficient is in this sense the best approximation given the modal amplitudes of the velocity field. Most important for the purpose of the present discussion, we have now tied the postulated linear dependence of the lift on the Fourier coefficients of the oscillatory fluctuations to an analytic derivation from the Navier–Stokes equation.

8. Conclusions

We have proposed a low-dimensional Galerkin model for the flow around a high-lift configuration. This model provides the least-order representation of periodic fluctuations using a single pair of POD modes per frequency. The novelty in this model lies in the inclusion of modes representing mean-field variations due to natural and actuated fluctuations. These modes are the key enabler for capturing the attenuating effect of high-frequency actuation on the natural instability. Thus, the mean-field model explains the mediation between the fluctuations at the natural and the actuated frequencies. The modelling approach is schematically illustrated in figure 13.

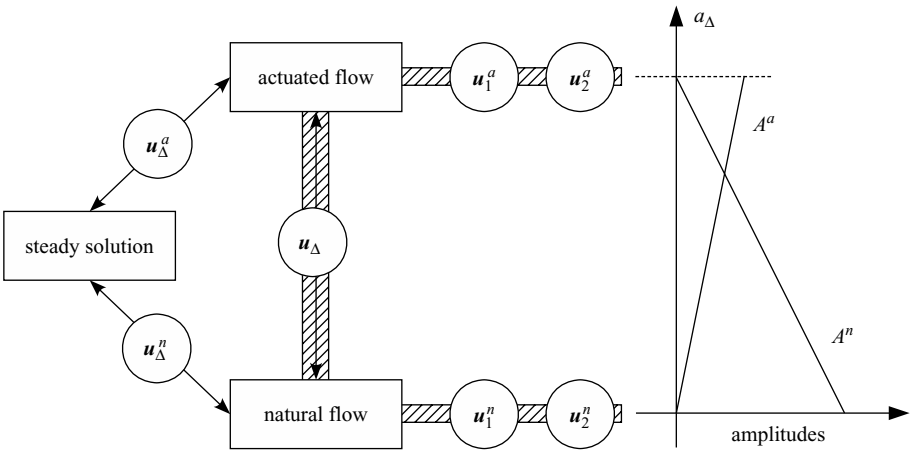

FIGURE 13. Principal sketch of the generalized mean-field model. The considered equilibrium flow states include the steady solution, natural and actuated flow (rectangles). The transitions are denoted by double arrows. The required Galerkin modes for each state are indicated by the circles. The grey rectangles connect the modes employed for the transients between the natural and actuated flow. The amplitudes for slowly varying transition between both states are depicted on the right side.

Dynamics covered by the model include natural vortex shedding, the effect of high-frequency forcing, as well as actuated and un-actuated transients based on URANS data. The model captures the original URANS simulation surprisingly well considering the very low order. The phase relation of flow and actuation of the URANS and least-order Galerkin model data is in good agreement. This agreement is important for flow control design. Model predictions include the lift coefficient which is also in good agreement with the original data. As can be expected, predictions by this least-order model erode during fast transients, and more accurate representation requires higher-order models. This applies, in particular, to prediction of the lift coefficient during fast transients.

The developed model generalizes existing mean-field theory by including an additional frequency. It is straightforward to include more frequencies if the assumptions in §§ 4 and 5.3 hold correspondingly. From figure 13, this can be conceptualized by including a row that describes an additional 'flow operating condition' with corresponding oscillatory and shift-modes. This modelling approach is expected to work for flows that are dominated by coherent structures. A main advantage of the analytical model is the possibility of a simple and robust calibration of a given data set. Thus, the low-dimensional model can be used as a quick test-bed for explanatory studies in simulation and experiment. It can, for instance, be used for improvement of open-loop control, observer design and sensor placement. The results are very encouraging for multi-frequency systems and the authors are pursuing the approach also for experimental data. Moreover, the discussed mechanism for high- and multi-frequency actuation is embedded in a recent finite-time thermodynamics formalism for fully nonlinear, infinite horizon attractor control (Noack *el al.* 2008).

The authors acknowledge the funding and excellent working conditions of the Collaborative Research Centre (Sfb 557) 'Control of complex turbulent shear flows' which is supported by the Deutsche Forschungsgemeinschaft (DFG) and hosted at the Berlin Institute of Technology. The work has been funded by the DFG under

grants NO 258/1-1 and 258/2-3 and the Centre National de la Recherche Scientifique (CNRS). The work of G. Tadmor was partially supported by NSF grants 0410246 and 0524070 and the US AFOSR grants FA9550-05-1-0399 and FA9550-06-1-0373. We appreciate valuable stimulating discussions with Laurent Cordier, Marek Morzyński, Frank Thiele and Jose-Eduardo Wesfreid as well as the local TU Berlin team: Katarina Aleksic, Oliver Lehmann, Nikolas Losse, Mark Pastoor, Michael Schlegel, Jon Scouten and Olaf Wiederhold. We are grateful for outstanding hardware and software support by Lars Oergel and Martin Franke. Last but not least, we thank the referees for their thoughtful and helpful suggestions.

Appendix A. Window filters

Here, we describe a general approach to split up the Navier–Stokes equations into separate equations for each flow contribution in partition (4.6). In the following observation, we use the standard notation of $\mathscr{L}_{2loc}$. Specifically, given (an implicitly known) Hilbert space H, the space $\mathscr{L}_{2loc}$ is the linear space of measurable functions $f : \Re \mapsto H$ with the property that $f|_{[a,b]} \in \mathscr{L}_2[a,b]$ for all finite intervals, $-\infty < a < b < \infty$. For example, in the context of Navier–Stokes solutions, $H = \mathscr{L}_2(\Omega)$ is the space of velocity fields. The reason $\mathscr{L}_{2loc}$ is used is to allow periodic infinite time trajectories, which are not members of $\mathscr{L}_2$ of the infinite time axis.

Observation A.1. *Let $f(t) \in \mathscr{L}_{2loc}$ satisfy assumption NSE 1:*

$$f(t) = f^B(t) + f^n(t) + f^a(t),$$

where f^B, f^n and f^a satisfy the counterparts of (4.8). Let $T > 0$ be a set length of a time window. Then there exist kernels $K^B(\tau)$, $K^n(\tau)$, $K^a(\tau) \in \mathscr{L}_2\left([-\frac{T}{2}, \frac{T}{2}]\right)$ such that the following approximation is satisfied to an order $O(\epsilon)$:

$$f^B(t) = \int_{-\frac{T}{2}}^{\frac{T}{2}} \mathrm{d}\tau\ K^B(\tau)\, f(t+\tau), \tag{A 1a}$$

$$f^n(t) = \int_{-\frac{T}{2}}^{\frac{T}{2}} \mathrm{d}\tau\ K^n(\tau)\, f(t+\tau), \tag{A 1b}$$

$$f^a(t) = \int_{-\frac{T}{2}}^{\frac{T}{2}} \mathrm{d}\tau\ K^a(\tau)\, f(t+\tau). \tag{A 1c}$$

The significance of Observation A.1 in the present discussion is that the window filters in (A 1) commute with time differentiation; when applied to the velocity field $\boldsymbol{u}(\boldsymbol{x}, t)$, the same holds for spatial derivatives. Hence, this filter has one important property of the Reynolds average (Monin & Yaglom 1971).

Proof. Denote $\boldsymbol{\Phi} \stackrel{\text{def}}{=} \{\Phi_i(\tau)\}_{i=1}^5 = \{1, \cos(\omega_n\tau), \sin(\omega_n\tau), \cos(\omega_a\tau), \sin(\omega_a\tau)\}$, and let $\boldsymbol{A} : \Re^5 \mapsto \mathrm{span}(\boldsymbol{\Phi}) \subset \mathscr{L}_2\{[-\frac{T}{2}, \frac{T}{2}]\}$ be defined as

$$\boldsymbol{A}\,\boldsymbol{d} = \sum_{i=1}^{5} d_i \Phi_i(\tau). \tag{A 2}$$

Then, the adjoint $\boldsymbol{A}^*$: span $(\boldsymbol{\Phi}) \mapsto \Re^5$ is an integral operator and the orthogonal projection of $\mathscr{L}_2\{[-\frac{T}{2}, \frac{T}{2}]\}$ onto $\mathrm{span}(\boldsymbol{\Phi})$ is $\boldsymbol{\Pi} \stackrel{\text{def}}{=} \boldsymbol{A}\,(\boldsymbol{A}^*\,\boldsymbol{A})^{-1}\,\boldsymbol{A}^*$. In particular, the

linear combination coefficients of the projection $\mathbf{\Pi}\,\zeta$ are given by integral functionals:

$$\boldsymbol{d} = \left(\boldsymbol{A}^* \boldsymbol{A}\right)^{-1} \boldsymbol{A}^* \zeta \quad \Leftrightarrow \quad d_i = \int_{-\frac{T}{2}}^{\frac{T}{2}} \mathrm{d}\tau \; K_i(\tau)\, \zeta(\tau), \tag{A 3}$$

where the kernels K_i are linear combinations of the base functions Φ_i. In the simple case where $\boldsymbol{T} = \boldsymbol{T}_n$ is the natural period and the two frequencies are harmonically related, this formulation reduces to a partial Fourier expansion and K_i are the standard normalized versions of the trigonometric functions.

Now let $f(t)$ be a time function satisfying NSE 1. This means that over a window $[t-\frac{T}{2},\ t+\frac{T}{2}]$ the three components of the function $\zeta(\tau) = f(t+\tau)$ can be approximated to an order $O(\epsilon)$ in the form

$$\begin{aligned} f^B(t+\tau) &= f^B(t), \\ f^n(t+\tau) &= \eta^n \; \cos(\omega_n \tau + \theta^n) \\ &= \eta^n \; [\cos(\theta^n) \; \cos(\omega_n \tau) - \sin(\theta^n) \; \sin(\omega_n \tau)]\,, \\ f^a(t+\tau) &= \eta^a \; \cos(\omega_a \tau + \theta^a) \\ &= \eta^a \; [\cos(\theta^a) \; \cos(\omega_a \tau) - \sin(\theta^a) \; \sin(\omega_a \tau)]\,. \end{aligned} \tag{A 4}$$

Each of the functions on the right-hand side of (A 4), as well as their sum, is a member of span($\mathbf{\Phi}$). Thus, we can approximate $\zeta(\tau) = f(t+\tau) = \boldsymbol{A}\,\boldsymbol{d}$ as in (A 2). The approximation is accurate up to an order $O(\epsilon)$ (say, relative to the $\mathscr{L}_2\,[-T/2, T/2]$ norm). The coefficients d_i are computed by integral filters, as in (A 3).

Since the three approximate expressions for $f^B(t+\tau)$, $f^n(t+\tau)$ and $f^a(t+\tau)$ in (A 4) are all continuously differentiable in τ, they can be evaluated at $\tau = 0$, leading to evaluating the coefficients d_i, $i = 1, 2, 4$ as $f^B(t) = d_1$, $f^n(t) = \eta^n \; \cos(\theta^n) = d_2$ and $f^a(t) = \eta^a \; \cos(\theta^a) = d_4$. The proof is complete by comparing these expressions with the expressions from (A 3). Notice that the values of d_i, $i = 3, 5$, are not needed to evaluate $f^n(t+\tau)$ and $f^a(t+\tau)$ at $\tau = 0$. □

It is observed that the proof remains valid when the spanning set $\mathbf{\Phi}$ is enlarged to include a predetermined number of higher and mixed harmonics of the two base frequencies, that are deemed non-negligible in the flow under consideration. This is valid because while $\mathbf{\Phi}$ is implicitly assumed linearly independent, we do not assume orthogonality of the base functions. The significance of this observation is that the projection formulas in (A 1) can be made to filter out additional harmonics due to the quadratic terms in the Navier–Stokes equations, as computed below.

Appendix B. Structure of the Galerkin system

Here, we derive the structure of the Galerkin system from (5.11), and the hypotheses made heretofore. These assumptions include NSE 1 to NSE 4, in the Navier–Stokes framework and their effect on the Galerkin system through Galerkin projection. Inaccuracies that result from the linearization (5.11*c*) are partially compensated for by the calibration of system parameters. This linearization leads to the linear dependence of $\boldsymbol{a}^B$ on $(A^n)^2 = \|\boldsymbol{a}^n\|^2$ and $(A^a)^2 = \|\boldsymbol{a}^a\|^2$, as stated in Observation B.1. The expression for $\boldsymbol{a}^B$ without that assumption includes higher-order terms in $(A^n)^2$ and $(A^a)^2$.

Equations (5.12) and (5.13) can be derived from (5.11*a*), (5.11*b*) and (5.11*c*) in a straightforward manner by a lengthy calculation exploiting the phase-invariance assumption. Here, we choose a more compact and insightful Hilbert-space consideration.

Observation B.1. *Under the assumptions stated above, there exists a* 2×2 *matrix* $\boldsymbol{A}^B$ *such that*

$$\boldsymbol{a}^B = \boldsymbol{A}^B \begin{bmatrix} (\boldsymbol{A}^n)^2 \\ (\boldsymbol{A}^a)^2 \end{bmatrix} \tag{B 1}$$

Note that $\boldsymbol{a}^B = 0$ at $\boldsymbol{A}^a = \boldsymbol{A}^n = 0$ since the steady Navier–Stokes solution serves as base flow.

Proof. By NSE 1 the base flow satisfies time-independent boundary conditions, whence the mean-flow deformation $\boldsymbol{u}^\Delta = \boldsymbol{u}^B - \boldsymbol{u}_s$ satisfies homogeneous boundary conditions. The linear mean-field deformation term in (4.10) reads

$$\nabla \cdot (\boldsymbol{u}^s \otimes \boldsymbol{u}^\Delta + \boldsymbol{u}^\Delta \otimes \boldsymbol{u}^s) - \nu \triangle \boldsymbol{u}^\Delta. \tag{B 2}$$

This linear operator with homogeneous boundary conditions has the counterpart linear term $\boldsymbol{L}(\boldsymbol{a}^B)$ in (5.11*c*). We stipulate that the operator (B 2) and the corresponding matrix $\boldsymbol{L}$ are non-singular, in agreement with empirical observations. Inverting that matrix, a linear expression for $\boldsymbol{a}^B$ in terms of $\boldsymbol{Q}(\boldsymbol{a}^n, \boldsymbol{a}^n) + \boldsymbol{Q}(\boldsymbol{a}^a, \boldsymbol{a}^a)$ is obtained.

The phase invariance hypothesis implies that the two quadratic terms $\mathbf{Q}(\boldsymbol{a}^n, \boldsymbol{a}^n)$ and $\boldsymbol{Q}(\boldsymbol{a}^a, \boldsymbol{a}^a)$ are both phase independent. They are therefore linearly determined by $(A^n)^2$ and $(A^a)^2$, respectively. □

Observation B.2. *Equation (5.11a) can be written in the form*

$$\frac{\mathrm{d}}{\mathrm{d}t}\boldsymbol{a}^n = \begin{bmatrix} \tilde{\sigma}^n & -\tilde{\omega}^n \\ \tilde{\omega}^n & \tilde{\sigma}^n \end{bmatrix} \boldsymbol{a}^n \tag{B 3}$$

where the state-dependent coefficients are of the form

$$\begin{aligned} \tilde{\sigma}^n &= \sigma^n - \sigma^{n,n}\,(A^n)^2 - \sigma^{n,a}\,(A^a)^2, \\ \tilde{\omega}^n &= \omega^n + \omega^{n,n}\,(A^n)^2 + \omega^{n,a}\,(A^a)^2. \end{aligned} \tag{B 4}$$

Proof. Clearly, the right-hand side of (5.11*a*) is linear in $\boldsymbol{a}^n$. It can therefore be re-written in the form

$$\frac{\mathrm{d}}{\mathrm{d}t}\boldsymbol{a}^n = F(\boldsymbol{a}^B)\,\boldsymbol{a}^n, \tag{B 5}$$

where the matrix $F(\boldsymbol{a}^B)$ depends on $\boldsymbol{a}^B$ in an affine manner. Invoking Observation B.1, the dependence on $\boldsymbol{a}^B$ may be substituted by dependence on $(A^n)^2$ and $(A^a)^2$. The fact that (B 5) is phase invariant means that the matrix F must commute with any rotation matrix. As such, it must be a scaled rotation matrix. That is, F must be of the form specified in (B 3). The affine dependence on the parameters implies (B 4). □

Observation B.3. *Equation (5.11b) can be written in the form*

$$\frac{\mathrm{d}}{\mathrm{d}t}\boldsymbol{a}^a = \begin{bmatrix} \tilde{\sigma}^a & -\tilde{\omega}^a \\ \tilde{\omega}^a & \tilde{\sigma}^a \end{bmatrix} \boldsymbol{a}^a + \begin{bmatrix} \kappa & -\lambda \\ \lambda & \kappa \end{bmatrix} \boldsymbol{b} \tag{B 6}$$

where the state-dependent coefficients are of the form

$$\begin{aligned} \tilde{\sigma}^a &= \sigma^a - \sigma^{a,n}(A^n)^2 - \sigma^{a,a}(A^a)^2, \\ \tilde{\omega}^a &= \omega^a + \omega^{a,n}(A^n)^2 + \omega^{a,a}(A^a)^2. \end{aligned} \tag{B 7}$$

The proof of this observation is completely analogous to the proof of Observation B.2 and is left out. This completes the derivation of (5.12) and (5.13) from (5.11*a*), (5.11*b*) and (5.11*c*).

REFERENCES

Amitay, M. & Glezer, A. 2002 Controlled transients of flow reattachment over stalled airfoils. *Intl J. Heat Transfer and Fluid Flow* **23**, 690–699.

Aubry, N., Holmes, P., Lumley, J. L. & Stone, E. 1988 The dynamics of coherent structures in the wall region of a turbulent boundary layer. *J. Fluid Mech.* **192**, 115–173.

Ausseur, J. M. & Pinier, J. T. 2005 Towards closed-loop feedback control of the flow over NACA-4412 airfoil. *AIAA Paper* 2005–0343.

Becker, R., King, R., Petz, R. & Nitsche, W. 2007 Adaptive closed-loop separation control on a high-lift configuration using extremum seeking. *AIAA J.* **45** (6), 1382–1392.

Bergmann, M., Cordier, L. & Brancher, J.-P. 2005 Optimal rotary control of the cylinder wake using proper orthogonal decomposition reduced order model. *Phys. Fluids* **17** (097101), 1–21.

Collis, S. S., Joslin, R. D., Seifert, A. & Theofilis, V. 2004 Issues in active flow control: theory, control, simulation, and experiment. *Prog. Aerosp. Sci.* **40**, 237–289.

Couplet, M., Sagaut, P. & Basdevant, C. 2003 Intermodal energy transfers in a proper orthogonal decomposition – Galerkin representation of a turbulent separated flow. *J. Fluid Mech.* **491**, 275–284.

Dušek, J., Le Gal, P. & Fraunié, P. 1994 A numerical and theoretical study of the first Hopf bifurcation in a cylinder wake. *J. Fluid Mech.* **264**, 59–80.

Favier, J., Cordier, L. & Kourta, A. In press Accurate POD reduced-order models of separated flows. *Phys. Fluids.*

Fletcher, C. A. J. 1984 *Computational Galerkin Methods*. Springer-Verlag.

Gad-el-Hak, M. 1996 Modern developments in flow control. *Appl. Mech. Rev.* **49**, 365–379.

Gad-el-Hak, M. 2000 *Flow Control: Passive, Active and Reactive Flow Management*. Cambridge University Press.

Galletti, G., Bruneau, C. H., Zannetti, L. & Iollo, A. 2004 Low-order modelling of laminar flow regimes past a confined square cylinder. *J. Fluid Mech.* **503**, 161–170.

Gerhard, J., Pastoor, M., King, R., Noack, B. R., Dillmann, A., Morzyński, M. & Tadmor, G. 2003 Model-based control of vortex shedding using low-dimensional Galerkin models. *AIAA Paper* 2003-4262.

Graham, W. R., Peraire, J. & Tang, K. Y. 1999 Optimal control of vortex shedding using low-order models. Part I: Open-loop model development. *Int. J. Num. Meth. Eng.* **44**, 945–972.

Günther, B., Thiele, F., Petz, R., Nitsche, W., Sahner, J., Weinkauf, T. & Hege, H. C. 2007 Control of separation on the flap of a three element high-lift configuration. *AIAA Paper* 2007-0265.

Henning, L., Pastoor, M., Noack, B. R., King, R. & Tadmor, G. 2007 Feedback control applied to the bluff body wake. In *Active Flow Control* (ed. R. King), Notes on Numerical Fluid Mechanics and Multidisciplinary Design, vol. 95, pp. 369–390. Springer-Verlag.

Holmes, P., Lumley, J. L. & Berkooz, G. 1998 *Turbulence, Coherent Structures, Dynamical Systems and Symmetry*. Cambridge University Press.

Hu, G.-H., Sun, D.-J., Yin, X.-Y. & Tong, B.-G. 1996 Hopf bifurcation in wakes behind a rotating and translating circular cylinder. *Phys. Fluids* **8**, 1972–1974.

Kaepernick, K., Koop, L. & Ehrenfried, K. 2005 Investigation of the unsteady flow field inside a leading edge slat cove. *AIAA Paper* 2005–2813.

King, R. (Ed.) 2007 *Active Flow Control*, Notes on Numerical Fluid Mechanics and Interdisciplinary Design, vol. 95. Springer-Verlag.

Ladyzhenskaya, O. A. 1963 *The Mathematical Theory of Viscous Incompressible Flow*. Gordon and Breach.

Luchtenburg, D. M., Tadmor, G., Lehmann, O., Noack, B. R., King, R. & Morzyński, M. 2006 Tuned POD Galerkin models for transient feedback regulation of the cylinder wake. *AIAA Paper* 2006-1407.

Maurel, A., Pagneux, V. & Wesfreid, J. E. 1995 Mean-flow correction as a non-linear saturation mechanism. *Europhysics Lett.* **32**, 217–222.

Monin, A. S. & Yaglom, A. M. 1971 *Statistical Fluid Mechanics I*. The MIT Press.

Noack, B. R. 2006 Niederdimensionale Galerkin-Modelle für laminare und transitionelle freie Scherströmungen (transl. Low-dimensional Galerkin models of laminar and transitional free shear flows). Habilitation thesis, Fakultät V – Verkehrs- und Maschinensysteme, Berlin Institute of Technology, Germany.

Noack, B. R., Afanasiev, K., Morzyński, M., Tadmor, G. & Thiele, F. 2003 A hierarchy of low-dimensional models for the transient and post-transient cylinder wake. *J. Fluid Mech.* **497**, 335–363.

Noack, B. R. & Copeland, G. S. 2000 On a stability property of ensemble-averaged flow. *Tech. Rep.* 03/2000. Hermann-Föttinger-Institut für Strömungsmechanik, Berlin Institute of Technology.

Noack, B. R. & Eckelmann, H. 1994 A low-dimensional Galerkin method for the three-dimensional flow around a circular cylinder. *Phys. Fluids* **6**, 124–143.

Noack, B. R., Papas, P. & Monkewitz, P. A. 2005 The need for a pressure-term representation in empirical Galerkin models of incompressible shear flows. *J. Fluid Mech.* **523**, 339–365.

Noack, B. R., Pelivan, I., Tadmor, G., Morzyński, M. & Comte, P. 2004*a* Robust low-dimensional Galerkin models of natural and actuated flows. In *Proceedings of the Fourth Aeroacoustics Workshop, RWTH Aachen, February 26–27, 2004* (ed. W. Schröder & P. Tröltzsch). Institut für Akustik und Sprachkommunikation, Technical University of Dresden.

Noack, B. R., Schlegel, M., Ahlborn, B., Mutschke, G., Morzyński, M., Comte, P. & Tadmor, G. 2008 A finite-time thermodynamics of unsteady fluid flows. *J. Non-Equilib. Thermodyn.* **33** (2), 103–148.

Noack, B. R., Tadmor, G. & Morzyński, M. 2004*b* Actuation models and dissipative control in empirical Galerkin models of fluid flows. In *Proceedings of the 2004 American Control Conference*, pp. 5722–5727. American Automatic Control Council (AACC), Dayton, OH, USA.

Noack, B. R., Tadmor, G. & Morzyński, M. 2004*c* Low-dimensional models for feedback flow control. Part I. Empirical Galerkin models. *AIAA Paper* 2004-2408.

Pastoor, M., Henning, L., Noack, B. R., King, R. & Tadmor, G. 2008 Feedback shear layer control for bluff body drag reduction. *J. Fluid Mech.* **608**, 161–196.

Pastoor, M., Noack, B. R., King, R. & Tadmor, G. 2006 Spatiotemporal waveform observers and feedback in shear layer control. *AIAA Paper* 2006-1402.

Raju, R. & Mittal, R. 2002 Towards physics based strategies for separation control over an airfoil using synthetic jets. *AIAA Paper* 2007-1421.

Rediniotis, O. K., Ko, J. & Kurdila, A. J. 2002 Reduced order nonlinear Navier–Stokes models for synthetic jets. *J. Fluids Engng* **124**, 433–443.

Rempfer, D. & Fasel, F. H. 1994 Dynamics of three-dimensional coherent structures in a flat-plate boundary-layer. *J. Fluid Mech.* **275**, 257–283.

Reynolds, W. C. & Hussain, A. K. M. F. 1972 The mechanics of an organized wave in turbulent shear flow. Part 3. Theoretical model and comparisons with experiments. *J. Fluid Mech.* **54**, 263–288.

Rowley, C. W. & Juttijudata, V. 2005 Model-based control and estimation of cavity flow oscillations. In *Proceedings of the 44th IEEE Conference on Decision and Control and European Control Conference*, pp. 512–517. European Union Control Association (EUCA), Saint-Martin d'Hères, France.

Rummler, B. 2000 Zur Lösung der instationären inkompressiblen Navier-Stokesschen Gleichungen in speziellen Gebieten (transl. On the solution of the incompressible Navier–Stokes equations in special domains). Habilitation thesis. Fakultät für Mathematik, Otto-von-Guericke-Universität Magdeburg.

Rung, T. & Thiele, F. 1996 Computational modelling of complex boundary layer flows. In *Proceedings of the 9th International Symposium on Transport Phenomena in Thermal-Fluids Engineering*, pp. 321–326. Singapore.

Samimy, M., Debiasi, M., Caraballo, E., Serrani, A., Yuan, X., Little, J. & Myatt, J. 2007 Feedback control of subsonic cavity flows using reduced-order models. *J. Fluid Mech.* **579**, 315–346.

Schatz, M., Günther, B. & Thiele, F. 2006 Computational investigation of separation control over high-lift airfoil flows. In *Active Flow Control* (ed. R. King), Notes on Numerical Fluid Mechanics and Multidisciplinary Design, vol. 95, pp. 260–278. Springer-Verlag.

Seifert, A., Darabi, A. & Wygnanski, I. 1996 On the delay of airfoil stall by periodic excitation. *J. Aircraft* **33** (4), 691–699.

Siegel, S., Cohen, K. & McLaughlin, T. 2003 Feedback control of a circular cylinder wake in experiment and simulation. *AIAA Paper* 2003-3569.

Siegel, S. G., Seidel, J., Fagley C., Luchtenburg, D. M., Cohen, K. & McLaughlin, T. 2008 Low-dimensional modelling of a transient cylinder wake using double proper orthogonal decomposition. *J. Fluid Mech.* **610**, 1–42.

Stuart, J. T. 1958 On the non-linear mechanics of hydrodynamic stability. *J. Fluid Mech.* **4**, 1–21.

Tadmor, G., Gonzalez, J., Lehmann, O., Noack, B. R., Morzyński, M. & Stankiewicz, W. 2007 Shift modes and transient dynamics in low order, design oriented Galerkin models. *AIAA Paper* 2007-0111.

Tadmor, G., Noack, B. R., Morzyński, M. & Siegel, S. 2004 Low-dimensional models for feedback flow control. Part II. Controller design and dynamic estimation. *AIAA Paper* 2004-2409.

Ukeiley, L., Cordier, L., Manceau, R., Delville, J., Bonnet, J. P. & Glauser, M. 2001 Examination of large-scale structures in a turbulent plane mixing layer. Part 2. Dynamical systems model. *J. Fluid Mech.* **441**, 61–108.

Zielinska, B. J. A., GoujonDurand, S., Dušek, J. & Wesfreid, J. 1997 Strongly nonlinear effect in unstable wakes. *Phys. Rev. Lett.* **79**, 3893–3896.